MIT/WHOI

Massachusetts Institute of Technology
Woods Hole Oceanographic Institution

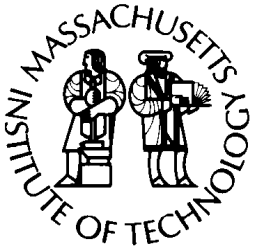

Joint Program in Oceanography/ Applied Ocean Science and Engineering

MASTER OF SCIENCE THESIS

Abyssal Mixing from Bottom Boundary Effects in Mid-Atlantic Ridge Flank Canyons

by

Rebecca Walsh Dell

June 2010

ABYSSAL MIXING FROM BOTTOM BOUNDARY EFFECTS IN MID–ATLANTIC RIDGE FLANK CANYONS

by

Rebecca Walsh Dell
A. B., Harvard University, 2005

Submitted in partial fulfillment of the requirements for the degree of

Master of Science

at the

MASSACHUSETTS INSTITUTE OF TECHNOLOGY

and the

WOODS HOLE OCEANOGRAPHIC INSTITUTION

June 2010

Signature of Author

Joint Program in Oceanography/Applied Ocean Science and Engineering
Massachusetts Institute of Technology
and Woods Hole Oceanographic Institution
30 January 2010

Certified By

Lawrence J. Pratt
Thesis Supervisor

Accepted By

Karl Helfrich
Chair, Joint Committee for Physical Oceanography
Massachusetts Institute of Technology
and Woods Hole Oceanographic Institution

Abstract

This paper begins to explore a previously neglected mechanism for abyssal ocean mixing using bottom boundary layer dynamics. Abyssal mixing and the associated upward buoyancy fluxes are necessary to balance the sinking of dense waters at high latitudes and to close the global overturning circulation. Previous studies have concentrated on the hypothesis that the primary mechanism for this mixing is breaking internal waves generated by tidal flows over rough topography. However, intriguing observations, particularly from the Brazil Basin Tracer Release Experiment, suggest that mixing in the flank canyons of the Mid–Atlantic Ridge generated when strong mean flows interact with the many sills and constrictions within the canyons may represent a dynamically important amount of abyssal mixing. The energy pathways and mechanisms of this mixing are much less clear than in the case of breaking internal waves. This study attempts to clarify this by suggesting an analogy with an idealized diffusive boundary layer over a sloping bottom. This boundary layer is characterized by up–slope flows powered by the buoyancy flux in the fluid far from the boundary. Here we explore the energy budget of the boundary layer, and find that the diffusive boundary layer provides flows that are generally consistent with those observed in submarine canyons. In addition, we derive the vertical velocity in the far–field fluid, analogous to an Ekman pumping velocity, that these boundary layers can induce when the bottom slope is not constant. Finally, we present both theoretical and numerical models of exchange flows between the bottom boundary and the far–field flow when the bottom slope is not constant. These exchange flows provide a mechanism by which boundary–driven mixing can affect the overall stratification and buoyancy fluxes of the basin interior.

Acknowledgements

I would like to acknowledge the patient and stimulating support of my advisor, Larry Pratt, throughout this work. I also enjoyed great insight and assistance from conversations with Tom Peacock, John Toole, Raffaele Ferrari, Rui Xin Huang, Jim Ledwell and Joe Pedlosky. Finally, I would like to thank my parents. During this work, I was supported by a NSF Graduate Research Fellowship.

1 Introduction

The hundreds of canyons on the bottom of the Atlantic ocean have seldom been carefully observed. However, what observations we do have show some interesting features, features that suggest that physical processes in these canyons may be rather more significant to the large–scale dynamics of the ocean basin than previously considered. First, they appear to have significant mean flows along the canyon axis, which contain more energy than the tidal frequency bands and often exceed the peak tidal velocities. These along-axis flows have been reported in both ridge–flank and ridge–crest canyons (Thurnherr et al., 2005; St. Laurent and Thurnherr, 2007; Thurnherr and Speer, 2003; Thurnherr et al., 2008). In the ridge–flank canyon at 22°S studied as part of the Brazil Basin Tracer Release Experiment (BBTRE) and shown in Figure 1, a current meter mooring deployed for two years found a mean along–axis current of 1.7 cm s^{-1} going up the slope of the Mid–Atlantic Ridge (Toole, 2007), notably fast for the bottom of the ocean. Typical peak tidal velocities measured by the current meter mooring were on the order of 2 cm s^{-1}. Furthermore, the current measured by the mooring was strongly bottom–intensified and confined within the canyon, as shown by the red arrows in Figure 1. The largest mean velocities were within 200 m of the bottom, while above the canyon walls, which extend approximately 1000 m up from the canyon floor, the measured velocities were not significantly different from zero. The current meter results are broadly corroborated by the dispersion of an inert tracer released in the BBTRE, which migrated approximately 2500 km along the canyon over the course of 14 months, suggesting a mean velocity of a few centimeters per second (Ledwell et al., 2000).

The second interesting feature of the flow in ocean bottom canyons is that they all seem to have highly enhanced levels of mixing, with reported levels of dissipation as high as 10^{-6} W kg^{-1}, and turbulent eddy diffusivities as high as 3×10^{-2} m^2 s^{-1} (Polzin et al., 1996; St. Laurent and Thurnherr, 2007). In the canyon studied in the BBTRE, the *mean* dissipation level was estimated to be 9.3×10^{-10} W kg^{-1} and the typical diffusivity was 4.3×10^{-3} m^2 s^{-1} (Thurnherr et al., 2005), and the study participants believe that mixing in the canyon may have been systematically undersampled (St. Laurent, personal

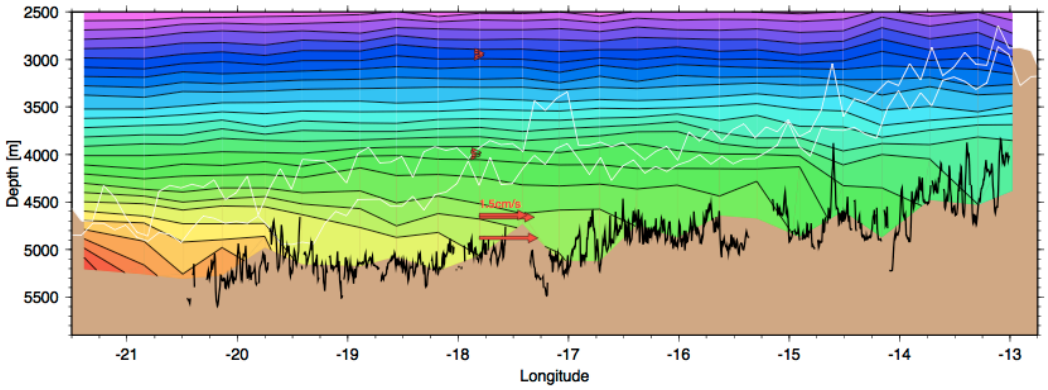

Figure 1: Hydrography section from the Brazil Basin Tracer Release Experiment, with mean velocities measured by a current meter mooring. These data were taken along the Mid–Atlantic Ridge flank canyon at 22°S indicated in Figure 2. Shaded contours show density, the thick black line gives the high resolution multi–beam bathymetry along the canyon axis, and the faint white lines are the tops of the canyon walls. The higher wall is on the south side of the canyon. Notice how the lines of constant density curve down and intersect the topography along the ridge slope, implying a west–to–east pressure gradient. The red arrows show the mean velocity as measured by a current meter mooring deployed for approximately two years (Toole, 2007). Courtesy of Andreas Thurnherr.

communication). These values should be compared to the background levels in the ocean at mid–depth of 10^{-10} W kg^{-1} of turbulent dissipation, and a turbulent diffusivity of 10^{-5} m^2 s^{-1}. Both the diffusivity and the dissipation rate are enhanced by an order of magnitude or more in the canyons.

A third notable feature of these canyon flows is the apparent colocation of the highest levels of mixing and topographic sills that obstruct the along–canyon current. The often sparse data suggests that there may be spilling flows over these sills, and possibly even instances of hydraulic control (Thurnherr et al., 2005; St. Laurent and Thurnherr, 2007).

The most obvious explanation for the mean flows is that there exists an exogenous pressure gradient driving them, for example a pressure gradient between the denser water of the Brazil Basin and the lighter water of the Gulf of Guinea in the case of the 22°S canyon. However, most of the ridge flank and ridge crest canyons terminate in dead ends, blocking such larger–scale flows. Moreover, strong mean flows have been observed in canyons in many

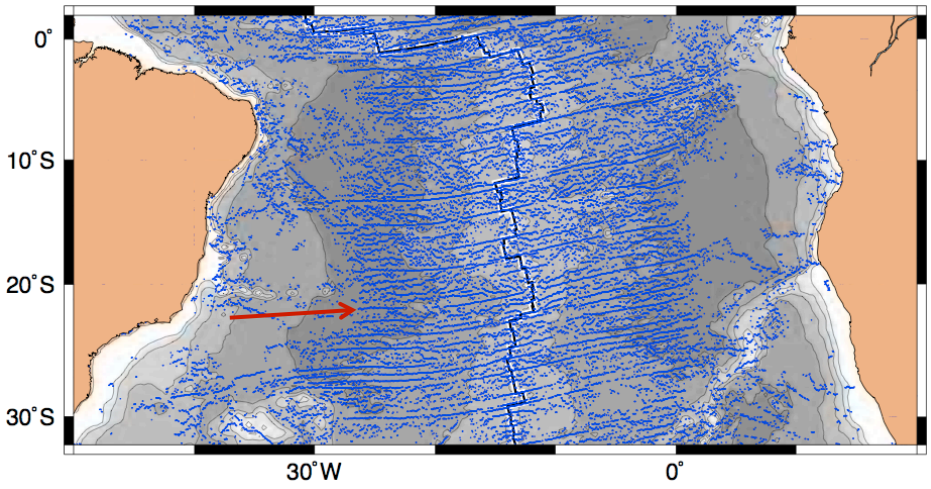

Figure 2: Distribution of canyons in the South Atlantic. Each dot on the above figure represents a local depth maximum. The Mid–Atlantic Ridge flank canyons are clearly show as roughly horizontal stripes extending on both sides of the ridge crest, indicated by a black line. These canyons are on the order of 20 km wide and 1000 m deep. They are crosscut by sills every 30–50 km. The canyon studied in the Brazil Basin Tracer Release Experiment is indicated by a red arrow. It is not particularly noteworthy. Courtesy of Andreas Thurnherr.

different orientations and contexts. As a result, local processes within the canyons are thought to be a more likely explanation of the flows observed.

Thurnherr and others who study these canyons have proposed that the strong mean flows, the enhanced levels of mixing, and the strong topographic interactions at the sills are not independent, but instead that the flow is in some sense 'mixing–driven'. The general picture of a mixing–driven flow is described by Thurnherr, et al.: "A fraction of the kinetic energy of externally imposed turbulence ... acts to increase the potential energy of the water column, while the remainder is dissipated. In a sloping valley this potential energy made available by mixing can drive a (restratifiying) up–valley flow" (2005). In the same paper, they point out that in the observed canyons "there is at least as much low–frequency [mean–flow] energy as tidal energy available for mixing." In Thurnherr's picture, the greater intensity mixing over the rough Mid–Atlantic Ridge relative to over the smooth–floored Brazil Basin (Polzin et al., 1997) causes the water column over the ridge to become more homogenized than the water column over the basin. This can be seen in Figure 1, as the isopycnals curve downward to the east and eventually intersect the bottom. This sets up a west–to–east pressure gradient, which in turn drives an up–slope flow. The flow goes down the pressure gradient and not across it (as geostrophic balance would predict) because of the topographic constriction of the canyon walls; the canyon is narrower than the local Rossby radius of deformation. Then this up–slope, along–canyon pressure–driven flow interacts with the rough topography of the ridge, possibly flowing over sills and obstructions in hydraulically interesting ways, to further enhance the mixing, reinforcing the dynamics of the system. As the mixing is enhanced, the up–slope flow accelerates, further enhancing mixing. This is an intuitively very appealing picture, but it raises some important questions, particularly: How can we describe the current as both the cause and the effect of the mixing? Is it possible for a flow to accelerate itself, or is this the fluid mechanical equivalent of perpetual motion?

This seeming paradox would be just a wet curiosity—albeit a rather interesting one—were it not for the passionate interest of physical oceanographers in where and how mixing occurs in the deep ocean. The reason physical oceanographers care so much about abyssal ocean mixing is that it

is a crucial part of the overturning circulation of the ocean and of the ocean's energy budget. We know that dense water masses like the Antarctic Bottom Water (AABW) and North Atlantic Deep Water (NADW) are formed near the poles and sink to the ocean depths, where they spread throughout the ocean basins of the world. However, many of these basins are closed—they have an abyssal inlet but no outlet. For example, the Brazil Basin has an abyssal inflow through the Vema Channel, but no abyssal outflow. Additionally, these deep waters are isolated from fluxes of heat or freshwater. The only way to export mass from the closed basins to balance the bottom water flowing into them is a net vertical and diapycnal velocity. This upward transport of mass occurs primarily by mixing heavier, deeper water with overlying lighter water. Hogg, et al., used this principle to estimate the average mixing rate in the Brazil Basin from hydrographic data (1982). In the Atlantic, the heaviest water is AABW, and it must mix with the overlying NADW to export mass from the closed abyssal basins. We have had a reasonable estimate of the total rate of mixing upward, called the diapycnal diffusivity, averaged over all of the world's ocean basins and over all depths below about 1000 m, since the 1960s, when Munk estimated it to be 10^{-4} m^2 s^{-1}, based on the mean density structure of the deep ocean (Munk, 1966). However, we also know that there is a high degree of spatial inhomogeneity in mixing rates, demonstrated most dramatically by the microstructure survey in the BBTRE that showed mixing enhanced by more than two orders of magnitude over the rough–bottomed flank of the Mid–Atlantic Ridge compared to the smooth–bottomed Brazil Basin interior (Polzin et al., 1997). Polzin and his coauthors ascribe this mixing to the breaking of internal waves generated by tidal flow over the rough bottom. However, a homogeneous internal wave field would not explain why the mixing inside the canyons is so much stronger—five times stronger—than above the equally rough flanks of the ridge. This is one reason why Thurnherr, et al., think the mixing is more likely caused by interactions between mean flows and topography inside the canyon.

Thurnherr, et al., suggest that if the data collected in the BBTRE are representative of the mixing rates found in other Mid–Atlantic Ridge canyons, the contribution of these canyon–related processes to the overall energy and

Region	Area	Dissipation (W kg^{-1})	Mixing
Abyssal Plain	40%	0.9×10^{-10}	14%
Above MAR flank	45%	1.9×10^{-10}	33%
Inside Canyons	15%	9.3×10^{-10}	53%

Table 1: Relative contributions to abyssal mixing by various types of topography in the Brazil Basin. For each class of topography, the area covered by that class is given, as is the mean diffusivity observed over that class of topography, and the percent of the total diffusivity in the Brazil Basin that represents. Data from Thurnherr, et al., (2005), Table 1, based on BBTRE microstructure surveys. These data reflect only mixing below 2000 m depth. Morris, et al. (2001) , divides the area into similar topographic classes to estimate the total mixing in the Brazil Basin, and finds results consistent with this and with heat budgets like those in Hogg, et al. (1982).

buoyancy budgets of the Atlantic ocean may be substantial. Table 1 gives estimates of the approximate contributions to abyssal mixing of three different classes of area, separated by the topographic class each contains. Figure 2 shows the ridge–flank canyons throughout the tropical South Atlantic. Only about 15% of the interface between the AABW and NADW occurs inside these canyons, but the mixing rates inside the canyons are so enhanced that as much as half of the mixing across this interface may take place in these canyons. Extrapolating from sparse observations is dangerous, but the BBTRE canyon is in many ways indistinguishable from nearly 1000 other Mid–Atlantic Ridge flank canyons. Both its topographic and hydrographic properties appear to be representative. All slow–spreading mid–ocean ridges are characterized by flank canyons approximately 1000 m deep and approximately 20 km wide. The mean slope of the Mid–Atlantic Ridge flanks is on the order of $10^{-3} - 10^{-2}$. The along–canyon pressure gradient observed in the BBTRE canyon is similar to that in other canyons as indicated by two meridional WOCE sections (A15 and A16) along the western flank of the Mid–Atlantic Ridge. There is no obvious reason why this canyon should be unlike the other canyons seen in Figure 2.

If the BBTRE canyon is typical of ridge flank canyons, and the rough mixing estimates based on the BBTRE data shown in Table 1 are reasonable, mixing in abyssal canyons could have potentially large implications for the way we understand and model ocean dynamics. The topographic mech-

anisms involved in canyon–mixing, like overflows, constrictions, and possibly hydraulic control, are very different than the mechanisms we usually use to explain abyssal mixing, like the breaking of internal waves. If our understanding of the mechanisms and location of deep ocean mixing changes, our understanding of the ocean's energy budget must change with it. After all, mixing is nothing more than converting kinetic and internal energy into potential energy. As a result, the real interest in these canyons is in understanding how they fit into the ocean's energy budget. What are the sources of energy that drive the observed dynamics, and what mechanisms convert that energy to new forms? Is it sensible to think about the mean flow as 'mixing driven,' and is the mixing that is generated by the mean flow significant? How much of the total abyssal upwelling can be accounted for by up slope flow in the canyons? Most generally, how is abyssal stratification maintained, and are canyon processes important to it? These are the central questions that this study seeks to begin to answer.

Specifically, this study will try to gain insight into some simple mechanisms that may be relevant to it by studying some highly idealized topographies. The main mechanism studied is diffusion–driven flow, first described by Phillips (1970) and Wunsch (1970) in the early 1970s. This is the best–established mechanism by which mixing can drive currents along sloping bottoms, a key feature of the observed canyon flows. We will explore the energetics of these flows in section 2, followed by an extension of the boundary layer theory to varying slopes in section 3, and finally present some numerical experiments of idealized configurations performed using the Regional Ocean Modeling System (ROMS) in section 4.

2 Theory: Energetics of Boundary Layer

The first goal in understanding the energetics of the Mid–Atlantic Ridge canyon system described in the introduction is to understand the energetics of our idealized model system. We begin with diffusion–driven flow over a constant non–rotating slope, as described by Phillips (1970) and shown in Figure 3. We assume that the solid bottom boundary is not a source of

heat or salt for the fluid, that is that the bottom is insulating. Since heat and salt diffuse down gradients, if there is no flux of heat or salt from the boundary, the slope–normal gradient of their concentration must go to zero at the boundary. This no–flux boundary condition at the sloping boundary causes isopycnals to bend downward to intersect the slope at a right angle, as shown in Figure 3. This in turn creates a left–to–right pressure force because denser fluid is at the same depth as lighter, and this leads to an upslope flow.

This system is governed by incompressible Boussinesq dynamics, which means that we assume the changes in density are much smaller than some constant background density ρ_0. We make the assumption $\rho = \rho_0$ everywhere in our dynamical equations except in the density equation and the gravitational terms of the momentum (Navier–Stokes) equations. This gives the following momentum equation:

$$\rho_0 \frac{\partial \underline{u}}{\partial t} + \rho_0 \underline{u} \cdot \nabla \underline{u} = -\nabla \tilde{p} + \tilde{\rho} \nabla \phi + \rho_0 \nabla \cdot (\nu \nabla \underline{u}) \tag{1}$$

ϕ is the gravitational potential, where $\underline{g} = \nabla \phi$ is the acceleration due to gravity. $\tilde{\rho}$ is the departure of the density ρ from a constant reference density ρ_0, and $\tilde{p}$ is the departure from the background hydrostatic pressure field $p_0 = p_{surface} - \rho_0 g z$. $\tilde{\rho}$ includes variations in density due to both the background stratification and the boundary layer effects. This version of the Navier–Stokes equations omits terms for rotation; this is applicable in canyons like the one observed in the BBTRE because the canyons are narrower than the local Rossby radius. The momentum equation (1) is coupled to a density equation:

$$\frac{\partial \tilde{\rho}}{\partial t} + \underline{u} \cdot \nabla \tilde{\rho} = \nabla \cdot (\kappa \nabla \tilde{\rho}) \tag{2}$$

This equation comes from combining the heat equation, the salt equation, and the conservation of mass under the Boussinesq approximation. We begin with a model system that has a constant stratification, constant slope, constant mixing coefficients κ and ν, and infinite extent in the along–slope direction. When Phillips first derived the solution for this case, he was imagining water flowing through fissures in rocks, where the relevant mixing co-

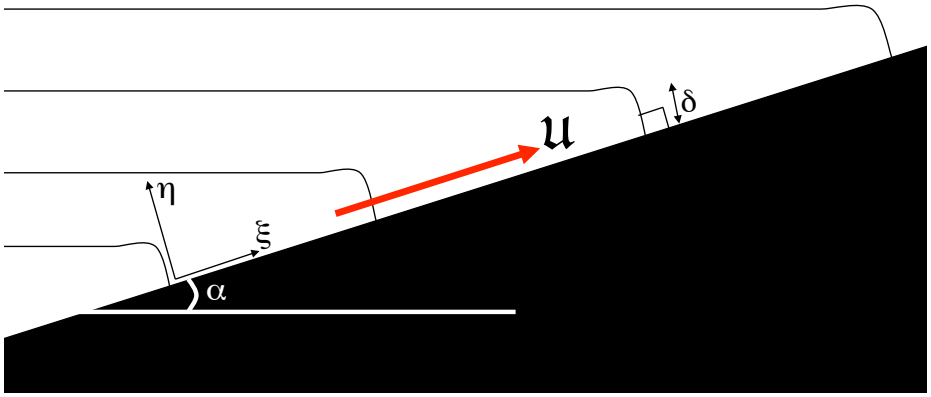

Figure 3: Definition of variables for theory section of paper. Key variables are α, the slope angle; $\delta = \frac{1}{\gamma}$, the boundary layer thickness scale; (ξ, η) the along–slope and slope–normal coordinates; and $\mathfrak{u}$, the along–slope velocity, indicated by the red arrow. The thin black lines are surfaces of constant density.

efficients would be the molecular viscosity ν_m and diffusivity κ_m. However, in the ocean, the background level of turbulence caused by winds and tides leads to a much higher rate of mixing. This enhanced mixing is customarily described using eddy mixing coefficients, ν_{eddy} and κ_{eddy}. This simplification discards any Stokes' drift that the turbulence might cause, but otherwise is thought to reasonably reflect the average influence of turbulence on scales larger than the individual eddies (Vallis, 2006). The following derivation is consistent either for molecular or for eddy mixing coefficients. When we compare its results to oceanic observations, or perform numerical experiments, we will use eddy mixing values for ν and κ. One of the most interesting aspects of the dynamics posited by Thurnherr is that the mixing coefficients ν and κ are themselves functions of the velocity field. However, the following theory requires that ν and κ have values that are known a priori, regardless of whether those are molecular or eddy values.

Under the simplifying assumptions of constant–slope, constant background stratification, and infinite extent, the most natural coordinates to use are an along–slope coordinate ξ and a slope–normal coordinate η, instead of horizontal and vertical coordinates. We associate an along–slope velocity $\mathfrak{u}$ and a slope–normal velocity $\mathfrak{w}$ to the coordinates (ξ, η). In this case, the problem

reduces to a one–dimensional system that varies only in the slope–normal η direction. $\frac{\partial}{\partial \xi} = 0$ for all the boundary layer variables. However, the density $\tilde{\rho}$ and pressure $\tilde{p}$ will still contain a term that varies with ξ because the density and pressure vary with the background stratification. Since there is no along–slope variation in the along–slope velocity, the no normal flow boundary condition at the bottom boundary implies that the slope–normal velocity $\mathfrak{w} = 0$ throughout the domain. Because of this, and because $\mathfrak{u}$ is independent of ξ, the nonlinear advection terms are precisely zero, so it is not necessary to assume linearity in the constant–slope, constant–stratification case. Finally, we seek a steady–state solution, where $\frac{\partial}{\partial t} = 0$, and we assume the mixing coefficients κ and ν are constant. This reduces our governing equations (1) to:

$$0 = -\frac{\partial \tilde{p}}{\partial \xi} - \tilde{\rho} g \sin\alpha + \rho_0 \nu \frac{\partial^2 \mathfrak{u}}{\partial \eta^2} \tag{3}$$

$$0 = -\frac{\partial \tilde{p}}{\partial \eta} - \tilde{\rho} g \cos\alpha \tag{4}$$

Similarly, the density equation (2) reduces to:

$$\mathfrak{u} \frac{\partial \tilde{\rho}}{\partial \xi} = \kappa \left(\frac{\partial^2 \tilde{\rho}}{\partial \xi^2} + \frac{\partial^2 \tilde{\rho}}{\partial \eta^2} \right) \tag{5}$$

Our boundary conditions are that the velocity must go to zero at the bottom (no–slip), the slope–normal density gradient must be zero at the bottom boundary, and that the along–slope velocity and density perturbations induced by the boundary must decay as you move far from the boundary:

$$\mathfrak{u}, \frac{\partial \tilde{\rho}}{\partial \eta} = 0 \quad , \quad \text{at } \eta = 0 \tag{6}$$

$$\mathfrak{u} \to 0 \quad , \quad \text{as } \eta \to \infty \tag{7}$$

$$\tilde{\rho} \to -\frac{N^2 \rho_0 z}{g} \quad , \quad \text{as } \eta \to \infty \tag{8}$$

Phillips solves this system by combining equations (3), (4), and (5), and obtaining a single fourth–order, constant–coefficient ordinary differential equation equation for the density perturbation. This in turn implies an along–

slope velocity, $\mathfrak{u}$:

$$\mathfrak{u}(\eta) = 2\kappa\gamma \cot\alpha e^{-\gamma\eta} \sin\gamma\eta \tag{9}$$

The along–slope velocity $\mathfrak{u}$ depends on η, the slope–normal coordinate, and α, the slope angle. It also depends on the thickness scale of the boundary layer, given by:

$$\delta = \frac{1}{\gamma} = \left(\frac{4\nu\kappa}{N^2 \sin^2\alpha}\right)^{\frac{1}{4}} \tag{10}$$

Higher rates of mixing ν and κ are associated with thicker boundary layers. A typical theoretical velocity profile is shown by the dashed line in Figure 7. It features a strong up–slope bottom current with a small down–slope flow above it. The down–slope component has less than 5% the volume flux of the primary up–slope current. The density field that supports the velocity given in equation (9) is:

$$\rho = \rho_0 - \rho_0 \frac{N^2}{g}(\xi \sin\alpha + \eta\cos\alpha) - \rho_0 \frac{N^2 \cos\alpha}{\gamma g} e^{-\gamma\eta}\cos\gamma\eta \tag{11}$$

This density field is split into an average density, ρ_0, a background stratification $\bar{\rho}$ given in the second term and having buoyancy frequency N^2, and a perturbation from that background stratification ρ' induced by the no flux condition at the boundary, given in the last term. $\tilde{\rho} = \bar{\rho} + \rho'$. Wunsch simultaneously obtained essentially the same solution using boundary layer approximations, but it turns out that his asymptotic approximations are unnecessary in the case of the truly constant and infinite slope (1970). However, as the slope angle α approaches zero, the time scale and length scale required for the flow to adjust to a steady–state solution both go to infinity. The time scale τ is given by the time required for diffusion to act across the thickness of the boundary layer:

$$\tau \sim \frac{\delta^2}{\kappa} \sim \frac{\sqrt{\mathscr{P}_r}}{N \sin\alpha} \tag{12}$$

$\mathscr{P}_r$ is the Prandtl number, $\frac{\nu}{\kappa}$. The adjustment length scale λ is given by the boundary layer velocity scale and τ:

$$\lambda \sim \mathfrak{u}\tau \sim \delta \cot\alpha \sim \frac{(\kappa\nu)^{1/4}}{N^{1/2}} \frac{\cos\alpha}{\sin^{3/2}\alpha} \tag{13}$$

For small angles, $\tau \sim \alpha^{-1}$ and $\lambda \sim \alpha^{-3/2}$. As the slope angle α decreases, the boundary layer thickness δ increases. If α continues to decrease, it will take longer and longer for diffusion to act across the increasing boundary layer thickness, so the boundary layer approaches a steady state more slowly. Though the solution presented in equations (9) and (11) is formally valid for all slope angles α, the solution is not expected to ever be observed for very small angles, because of the long space and time scales required to achieve steady state.

To construct an energy budget for this system, it's useful to begin with the full momentum equations used to derive the solution, the Boussinesq Navier–Stokes equations (1), and then apply our simplifying assumptions. These equations are multiplied by $\underline{u}$, the velocity to make a kinetic energy budget:

$$\underline{u} \cdot \left(\rho_0 \frac{\partial \underline{u}}{\partial t} + \rho_0 \underline{u} \cdot \nabla \underline{u} = -\nabla \tilde{p} + \tilde{\rho} \nabla \phi + \rho_0 \nabla \cdot (\nu \nabla \underline{u}) \right) \tag{14}$$

The kinetic energy is $KE = \frac{1}{2} \rho_0 \underline{u} \cdot \underline{u}$. Some rearranging gives:

$$\frac{\partial}{\partial t} (KE) + \underline{u} \cdot \nabla (KE) = -\nabla \cdot (\underline{u} \tilde{p}) - \tilde{\rho} \underline{u} \cdot \nabla \phi + \nabla \cdot (\nu \nabla (KE)) - \varepsilon \tag{15}$$

ε is the dissipation of kinetic energy, that is its transformation into heat:

$$\varepsilon = \rho_0 \nu \nabla \underline{u} : \nabla \underline{u} = \rho_0 \nu \left(\left(\frac{\partial u}{\partial x} \right)^2 + \left(\frac{\partial u}{\partial y} \right)^2 + \cdots + \left(\frac{\partial w}{\partial y} \right)^2 + \left(\frac{\partial w}{\partial z} \right)^2 \right) \tag{16}$$

In words, the time rate of change of kinetic energy is given by the combination of the kinetic energy advective flux divergence, the pressure work done by the flow, the conversion of potential energy into kinetic energy, the diffusive flux divergence of kinetic energy, and the dissipation of kinetic energy. We can similarly use the density equation (2) to derive a potential energy budget by taking $\phi \cdot (2)$:

$$\frac{\partial}{\partial t} (PE) + \underline{u} \cdot \nabla (PE) = \tilde{\rho} \underline{u} \cdot \nabla \phi + \nabla \cdot (\kappa \phi \nabla \tilde{\rho}) - \kappa \nabla \phi \cdot \nabla \tilde{\rho} \tag{17}$$

Potential energy is defined as $PE = \tilde{\rho} \phi$. In words, the time rate of change of

KE1	$\frac{\partial}{\partial t}(KE)$	Time Rate of Change of KE
KE2	$\underline{u} \cdot \nabla (KE)$	Advective Flux of KE
KE3	$-\nabla \cdot (\tilde{p}\underline{u})$	Divergence of Pressure Work
KE4	$-\tilde{\rho}\underline{u} \cdot \nabla \phi$	Conversion of PE $\rightarrow$ KE
KE5	$\nabla \cdot (\nu(\nabla(KE))$	Diffusion of KE
KE6	$-\nu\rho_0 \nabla \underline{u} : \nabla \underline{u}$	Viscous Dissipation (KE $\rightarrow$ IE)
PE1	$\phi \frac{\partial \tilde{\rho}}{\partial t}$	Time Rate of Change of PE
PE2	$-\underline{u} \cdot \nabla (PE)$	Advective Flux of PE
PE3	$\nabla \cdot (\kappa \phi \nabla \tilde{\rho})$	PE Diffusion
PE4	$\tilde{\rho}\underline{u} \cdot \nabla \phi$	Conversion of KE $\rightarrow$ PE
PE5	$-\kappa \nabla \phi \cdot \nabla \tilde{\rho}$	Conversion of IE to PE, or the Vertical Buoyancy Flux

Table 2: Terms in general Boussinesq Kinetic and Potential Energy budgets. Not all of these terms are relevant in a diffusive boundary layer. IE is internal energy, that is, heat.

potential energy is given by the combination of the potential energy advective flux divergence, the conversion of potential energy to kinetic energy, the diffusive flux divergence of potential energy, and the mixing–driven buoyancy flux. All of the terms in both the KE and PE budgets are summarized in Table 2.

So far, this describes a local energy balance. The way in which the energy terms balance one another at different heights above the bottom is shown in Figure 4. Close to the bottom, where the velocity shear is largest, the primary balance is between viscous dissipation and the diffusion of kinetic energy, while the mass fluxes in the potential energy budget must go to zero at the bottom. Far from the boundary, those mass fluxes are the only non–zero terms. The green lines, equal and opposite in the two subplots, show the net conversion of potential energy to kinetic. To find the net effect of the various terms, consider an integral budget over a fixed volume, taken without loss of generality to be given by $\xi \in (0, \xi_1)$, and $\eta \in (0, \eta_f)$. We take the limit as $\eta_f \rightarrow \infty$ to ensure that all boundary layer effects are captured by our budget. This volume is similar to the box shown as a dashed line in Figure 6, but with a constant bottom slope. The results of the integral budget are in Table 3.

What we can see is that the energy in the boundary layer is generated as potential energy, then converted to kinetic energy, then dissipated. The only

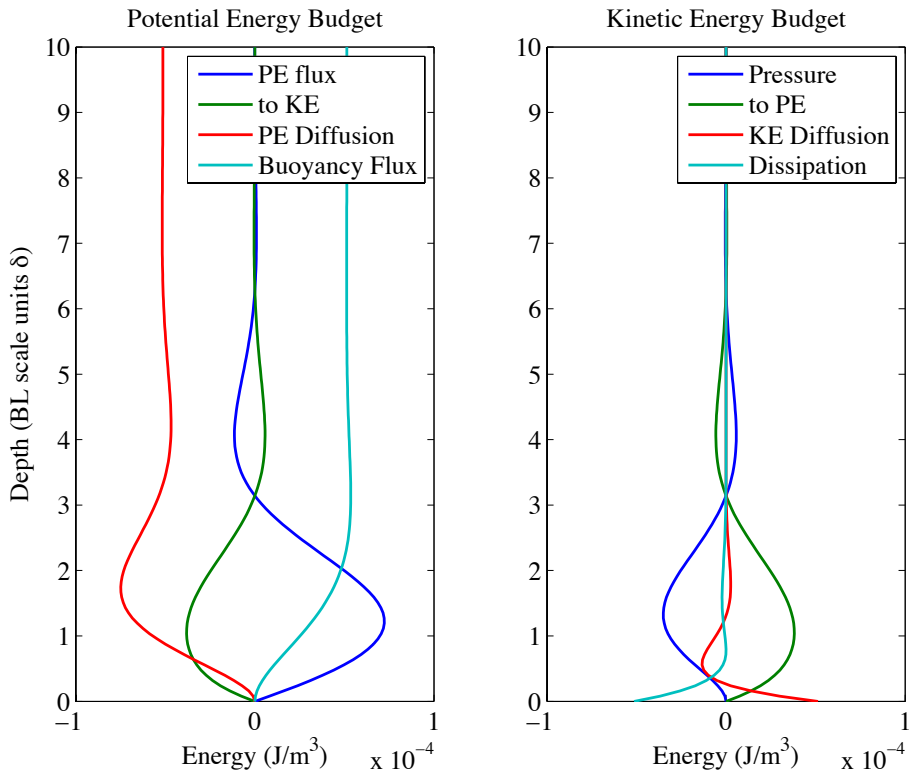

Figure 4: All terms contributing to the kinetic and potential energy budgets of a diffusive boundary layer over a sloping bottom. The vertical coordinate has units of the boundary layer thickness $\delta = \frac{1}{\gamma}$ defined in equation (10). The top of the boundary layer is defined as the zero–crossing of the boundary layer velocity, at $\gamma\eta = \pi$. The terms and their physical interpretations are given in in Table 2. Note that the source of energy that drives the boundary layer is the buoyancy flux, which generates potential energy. This potential energy is transformed into kinetic energy, and the conversion is shown as the equal and opposite green lines in both plots. The parameter values used are typical to the best of our knowledge of submarine canyons: $\nu, \kappa = 10^{-3}\,\mathrm{m^2 s^{-1}}$; $N^2 = 10^{-5}\,\mathrm{s^{-2}}$; $\alpha = 0.02\,\mathrm{rad}$. The integral contribution of each term to the total energy budget is given in Table 3.

KE1	$= 0$	$= 0$
KE2	$= 0$	$= 0$
KE3	$= -\frac{A}{2}\cos\alpha\,(2\xi_1\cos\alpha + \gamma\xi_1^2\sin\alpha)$	< 0
KE4	$= \frac{A}{4}\cos\alpha\,(5\xi_1\cos\alpha + 2\gamma\xi_1^2\sin\alpha)$	> 0
KE5	$= 0$	$= 0$
KE6	$= -\frac{A}{4}\xi_1\cos^2\alpha$	< 0
PE1	$= 0$	$= 0$
PE2	$= \frac{A}{4}\xi_1\cos\alpha\,(9\cos\alpha + 4\gamma\xi_1\sin\alpha)$	> 0
PE3	$= -\frac{A}{4}\xi_1\,(4\gamma\eta_f + \gamma\xi_1\sin(2\alpha))$	< 0
PE4	$= -\frac{A}{4}\xi_1\cos\alpha\,(5\cos\alpha + 2\gamma\xi_1\sin\alpha)$	< 0
PE5	$= -\frac{A}{2}\xi_1\,(1 - 2\gamma\eta_f + \cos(2\alpha))$	> 0

Table 3: Total contribution of various terms in the Boussinesq energy budget to the steady, constant slope diffusive boundary layer. Each term was obtained by integrating the general Boussinesq energy budget from $\xi = 0$ to ξ_1 and from $\eta = 0$ to η_f, then taking the limit as $\eta_f \to \infty$. Note that there is no loss of generality associated with these limits of integration; they represent any section of the slope. The final column gives the sign of each term, indicating whether the associated physical process is a source or a sink of energy. The coefficient $A = \rho_0 N^2 \kappa/\gamma$.

kinetic energy source term is KE4, the conversion term from potential energy. Dissipation (term KE6) is a net energy sink, as is the pressure term (KE3). Pressure work is constantly being done on the flow as it moves through the stratified ambient.

The source of the potential energy is the mixing of density upward (or buoyancy downward, if you prefer), which happens throughout the fluid through the diffusivity κ. However, this generation of potential energy from the mixing up of dense fluid manifests itself in two ways: directly through the buoyancy flux term (PE5) and indirectly as an advective flux of PE (PE2). This advective flux term (PE2) expresses the tendency of the boundary layer flow to restratify the boundary region. In a closed system, an advective term could not be considered a source term; advection just moves energy around, but does not add to it or remove it from the system. However, this is an open system, which posits the existence of an infinite reservoir of stratified fluid, maintaining a fixed N^2 everywhere in the domain outside the boundary layer. In order to maintain this stratification, mass, and so potential energy, is constantly being fluxed from the infinite reservoir into the boundary layer

region. In steady state, this PE flux is exactly balanced by the diffusion of density, and the isopycnals remain stationary.

It is possible to calculate the efficiency Γ of the conversion between potential and kinetic energy directly using the integral forms of the terms in the energy equations, given in Table 3:

$$\Gamma = \frac{PE \rightarrow KE}{\text{Total PE Sources}} = \frac{PE4}{PE2 + PE5} = \frac{5\cos^2\alpha + 2\xi_1\gamma\sin\alpha\cos\alpha}{4\pi - 5\cos^2\alpha + 4\xi_1\gamma\sin\alpha\cos\alpha} \tag{18}$$

For the parameter values shown in Figure 4, which are within oceanographic range, $\Gamma \approx 0.5$. Γ approaches a maximum value of 0.66 as $\alpha \rightarrow 0$. This conversion efficiency only concerns the volume within the boundary layer, that is within a distance of $\pi\delta$ of the boundary. It is necessary to restrict the volume considered, because an infinite domain will generate an infinite amount of potential energy through the buoyancy flux in term PE5.

It is here that the utility of the diffusion–driven flow model for understanding canyon flows starts to become clear. When speculating about the upslope flows observed in the BBTRE, Thurnherr, et al. (2005), posit that mixing both drives and results from the flow, making it difficult to understand the energy source of the system. Using the energy budget just constructed, however, we can specify precisely what the energy flux into the system is, and where it comes from: buoyancy flux from diffusion of mass generates potential energy (term PE5); some of this potential energy is converted into kinetic energy (terms PE4 and KE4) and some of it diffuses away (term PE3). The velocity resulting from the pressure gradient tends to restratify the boundary layer, introducing an advective flux of potential energy (term PE2), while some of the kinetic energy is dissipated as heat or internal energy (term KE6). The subsequent dynamics of the system now have a clear energy source: the buoyancy flux in term PE5.

Let's consider what is actually happening when we say that the buoyancy flux in term PE5 is driving the flow in the boundary layer. Outside of the boundary layer, where the velocities in our idealized system to go zero, the only non–zero terms in the momentum or energy equations come from the constant diffusion of density in the stratified far field. There is a continuous flux of density up (or of buoyancy down, if you prefer) in the far field, given

by $\kappa N^2 \rho_0$. If N^2 and κ are constant, this flux is also constant, and it does not affect the stratification. However, approaching the bottom boundary, there will inevitably be a flux–divergence. Density will continue to mix upward, but at the boundary there is no mass coming from below to replace it. The upslope, and so upward, advective mass flux in the boundary layer replaces the mass being mixed up by diffusion in the interior. The way that the buoyancy flux in the interior controls the flow in the boundary layer can be seen very clearly if you integrate the density equation (2) from the boundary:

$$\int_0^\infty \left(\mathfrak{u} \frac{\partial \rho}{\partial \xi} + \cancel{\mathfrak{w}} \frac{\partial \rho}{\partial \eta} = \nabla \cdot (\kappa \nabla \rho) \right) \mathrm{d}\eta \tag{19}$$

Unlike in the derivation leading to the velocity field in equation (9), here it is not necessary to assume that the diffusivity κ is constant. Divide through by $\frac{\partial \rho}{\partial \xi}$, a constant depending on N^2, to find total volume flux in the boundary layer is given by:

$$Q = \int_0^\infty \mathfrak{u} \mathrm{d}\eta = -\frac{g}{\rho_0 N^2 \sin \alpha} \left(\kappa \nabla \rho \right) \Big|_0^\infty = \kappa_\infty \cot \alpha \tag{20}$$

The total volume flux Q in the boundary layer is determined by the diffusivity far from the boundary κ_∞. This is a general statement of the boundary layer flux, and it is independent of the structure of the diffusivity κ. If we introduce a bottom–intensified mixing $\kappa(\eta)$, it might change the velocity structure of the boundary layer flow, it cannot change the total volume flux in it. However, it should be noted that for this argument to be truly satisfying, it should be the mass flux and not the volume flux that is exclusively determined by κ_∞. The mass flux, which is derived in the next section, depends on Q and γ, the boundary layer thickness scale. γ is expected to vary depending on the structure of $\kappa(\eta)$, for example if κ is intensified close to the boundary. It is not solely determined by the topography and κ_∞, as Q is. This may be an artifact of the Boussinesq approximation, under which we only consider some variations in density, but it does not appear to be possible to derive a closed–form solution for the velocity field without making this approximation. It would be possible to test numerically if the mass flux M varies when slope–normal variations in diffusivity are introduced, but that is beyond the scope

of the current study.

Phillips, et al., attempted to model bottom–intensified mixing $\kappa(\eta)$ in the laboratory by oscillating a rough mat over a sloping bottom (1986). They found that bottom intensified mixing led to a recirculation, with a down–slope flow immediately overlying the up–slope boundary layer flow seen in the laminar case. Since the net boundary layer flux is constrained by the far–field buoyancy flux, this picture of a strong up–slope flow with its transport mostly cancelled by a somewhat weaker down–slope flow makes a great deal of intuitive sense.

It is difficult to compare the predicted flux to that observed in the 22°S canyon because almost nothing is known about the cross–canyon structure of the flow, and the current meter mooring had instruments deployed at only three depths in the bottom 1000 m of the water column. However, we can make a rough comparison of theory and observations, choosing a value of the diffusivity representative of either measurements in the interior of the canyon or the background level of mixing observed in the ocean thermocline:

$$\begin{aligned} \kappa_{canyon} &= 5 \times 10^{-3}\,\mathrm{m\,s^{-2}} \\ \kappa_{thermocline} &= 5 \times 10^{-5}\,\mathrm{m\,s^{-2}} \end{aligned}$$

For a single typical ridge–flank canyon that is 30 km across, these yield along–slope fluxes:

$$\begin{aligned} Q_{canyon} &= 1.5 \times 10^{5}\,\mathrm{m^3\,s^{-1}} = .15\,\mathrm{Sv} \\ Q_{thermocline} &= 1.5 \times 10^{3}\,\mathrm{m^3\,s^{-1}} \end{aligned}$$

A relevant comparison for these numbers is the total amount of upwelling required to close the global overturning circulation, estimated to be 25–30 Sverdrups (Wunsch and Ferrari, 2004), which matches the rate of deep water formation. There are on the order of 1000 canyons like this one in the global ocean, with bottom slopes in the range of $10^{-2} - 10^{-3}$, giving a total upwelling from κ_{canyon} of 1 Sv, and one hundredth of that for $\kappa_{thermocline}$. This suggests that the advective upwelling flux from diffusion–driven flow in Mid–Atlantic Ridge canyons is not sufficient to close the overturning circula-

tion. However, the strong currents close to the bottom boundary may cause additional upwelling of mass through diapycnal mixing.

Q_{canyon} is consistent with a flow of order 1 cm s^{-1} over a depth of 500 m, which is roughly what the current meter observed, while $Q_{thermocline}$ suggests a velocity much smaller than what was measured. One possible explanation for why the near–field diffusivity better matches the observations than κ_∞ is that there may be a return flow down the canyon almost as large as the up–slope flow measured by the current meter, analogous to the down–slope recirculation of the type Phillips, et al., described in the laboratory. Such a flow could be passing unobserved in the gap of over 500 m between the two deepest sets of current meters (at about 4900m and 4650m depth) and the third current meter depth above the bottom (at about 4000m depth) on the BBTRE mooring. St. Laurent, et al. (2001), predicted just such a recirculation used the BBTRE hydrography and microstructure data, prior to the recovery of the current meter data. Unfortunately, it is unclear how reliable their estimate of the mean flow field is, as they predicted peak velocities an order of magnitude slower than those seen by the current meter. The diffusive boundary layer can also be compared to the observations in terms of the boundary layer thickness. Using the ranges of parameter values measured in the BBTRE, including κ_{canyon}, the theory suggest a scale thickness of $\delta \sim$ 90–250 m, giving a boundary layer thickness of $\delta\pi \sim$ 300–800 m, consistent with what is observed in the slope of the isopycnals (Ledwell et al., 2000). κ_{canyon} provides a closer match between theory and observations, both in terms of boundary layer flux and boundary layer thickness.

The far–field constraint on the boundary layer given in equation (20) presents some problems when we shift our gaze from a laminar flow on a laboratory scale to turbulent, high Reynolds number flows like those in the ocean. We know that the mixing in the ocean is strongly bottom–intensified; we have direct observations of this, and the boundary–driven and topographic mixing mechanisms we're discussing are by their nature strongest near the boundary. Therefore, if we make a direct analogy between the two contexts, using the diffusivity measured in the canyons as a constant κ_{eddy} substituted in for the molecular κ in our boundary layer solution in equation (9), we will substantially over–estimate the boundary layer flux. The lower mixing

rates in the oceanographic far field mean less vertical density flux far from the boundary and therefore less density flux divergence near the boundary that the boundary layer mass flux must compensate for. It is important to recognize this shortcoming of the analogy between laminar and turbulent diffusive boundary layers. However, in the interests of simplifying the mechanism, we do not deal with this shortcoming in the current study. Instead, both the theory and numerics use an enhanced but constant κ to describe mixing processes, and the value of κ_{eddy} is chosen to best match our limited observations.

We have spent some time discussing the energetics of a diffusion–driven flow. However, this boundary layer still lacks some key oceanographically relevant features. The slope–normal velocity is zero, so the boundary flow does not interact with the fluid in the far–field, and any enhanced mixing in the boundary layer cannot affect the stratification of the far field in an open domain. As a result, this boundary layer cannot be expected to play an important dynamical role in the larger circulation. To provide a mechanism for the coupling of the boundary layer to the bulk of the fluid, in the next section we will discuss the behavior of diffusive boundary layers over varying slopes.

3 Theory: Behavior of Boundary Layer over Varying Topography

Previous studies of diffusion–driven flow (Phillips, 1970; Garrett et al., 1993; Peacock et al., 2004; Thorpe, 1987) have restricted their attention to boundary layers over constant slopes, and usually constant mixing coefficients κ, ν. However, the slope of the ocean bottom varies at all scales, with potentially interesting consequences. The foremost among these consequences arises from the slope dependence of the flux in the boundary layer. As shown in equation (20), the volume flux is proportional to $\cot \alpha$. Varying topography means that the flux in the boundary layer also varies along–slope, which means that fluid must be exiting or entering the boundary layer at changes in slope. Like an Ekman layer, where variations in stress force a vertical

velocity, here variations in slope force a vertical velocity.

The first step in relaxing the restriction to constant slopes is to think about boundary layers over 'slowly varying' slopes. A slope can be thought to vary slowly if the slope is locally constant, that is if slope varies so slowly that the constant slope boundary layer solution can be used at each point along it. The criterion for slow variations is traditionally taken to be $\delta << R$, where R is the radius of curvature of the slope. The bottom boundary of the Mid–Atlantic Ridge does not vary slowly with respect to the turbulent boundary layer, as the high–resolution topographic measurements of the canyon depth shown in Figure 1; the bottom slope may be slowly varying with respect to the laminar boundary layer. In the slowly varying case, we can use the continuity equation to solve for the vertical velocity:

$$\frac{\partial \mathfrak{u}}{\partial \xi} + \frac{\partial \mathfrak{w}}{\partial \eta} = 0 \tag{21}$$

Taking the solution for a constant slope given in equation (9), and allowing the slope angle to vary as $\alpha(\xi)$, we find:

$$\mathfrak{w}(\xi, \eta) = \int_0^\infty \frac{\partial}{\partial \xi} \left(2\kappa\gamma \cot\alpha e^{-\gamma\eta} \sin\gamma\eta \right) \mathrm{d}\eta \tag{22}$$

We can find the constant of integration by applying a no normal flow boundary condition: $\mathfrak{w} = 0$ at $\eta = 0$. All of the terms in $\mathfrak{w}(\xi, \eta)$ are proportional to $e^{-\gamma\eta}$ except that constant of integration, so outside the boundary layer, it is the only part of the slope–normal velocity that remains. It is given by:

$$\mathfrak{W}_\infty(\xi) = -\kappa \frac{\partial \alpha}{\partial \xi} \frac{1}{\sin^2 \alpha} \tag{23}$$

The slope–normal velocity is proportional to the rate of change of the slope angle, so it is proportional to the *second* derivative or curvature of the topography. In the small–angle limit relevant to the ocean, we can convert $\mathfrak{W}_\infty$ into a vertical velocity:

$$W_\infty(x) = -\kappa \frac{h''}{h'^2} \tag{24}$$

W_∞ is expressed in terms of a topographic height $h(x)$, where $\alpha = h'(x)$. The velocity induced by a simple exponential topography is shown in Figure 5. In

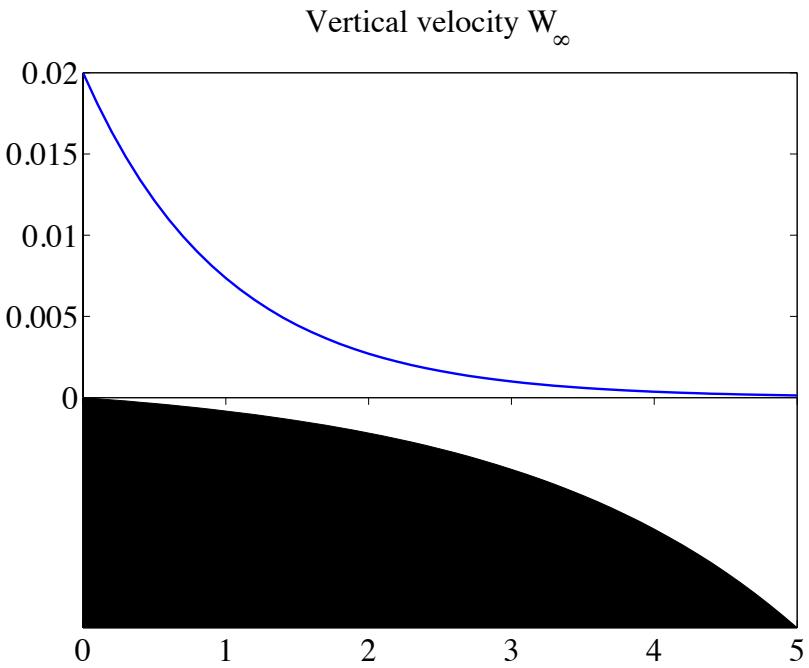

Figure 5: Vertical velocity induced over slowly varying topography. The model topography is shown in the lower panel, and the induced vertical velocity in the upper panel. Note the relationship of the induced vertical velocity to the curvature of the topography, as shown in equation (24).

this model, as you move toward the origin, the curvature of the topography increases, and so the velocity induced by the boundary layer increases. This vertical velocity, which exchanges fluid between the boundary layer and the far field has the potential to affect both the stratification and the circulation of the far field fluid. The effect on stratification is separate from the modification of stratification by the broadly distributed downwelling needed to balance the up–slope volume transport in the boundary layer (Woods, 1991).

Consider a topography consisting of two regions of constant slope with slope angles α_1 and α_2, as illustrated in Figure 6. Define $\xi = 0$ as the location of the change in slope. If $\alpha_1 < \alpha_2$, the volume flux in slope Region 1 will be larger than that in slope Region 2. Near the intersection of the two regions, we expect some of the boundary layer flux in Region 1 to be forced out of the boundary layer. This fluid will form an intrusion at its depth of neutral buoyancy. The mass flux in the intrusion will depend on the mass flux in the

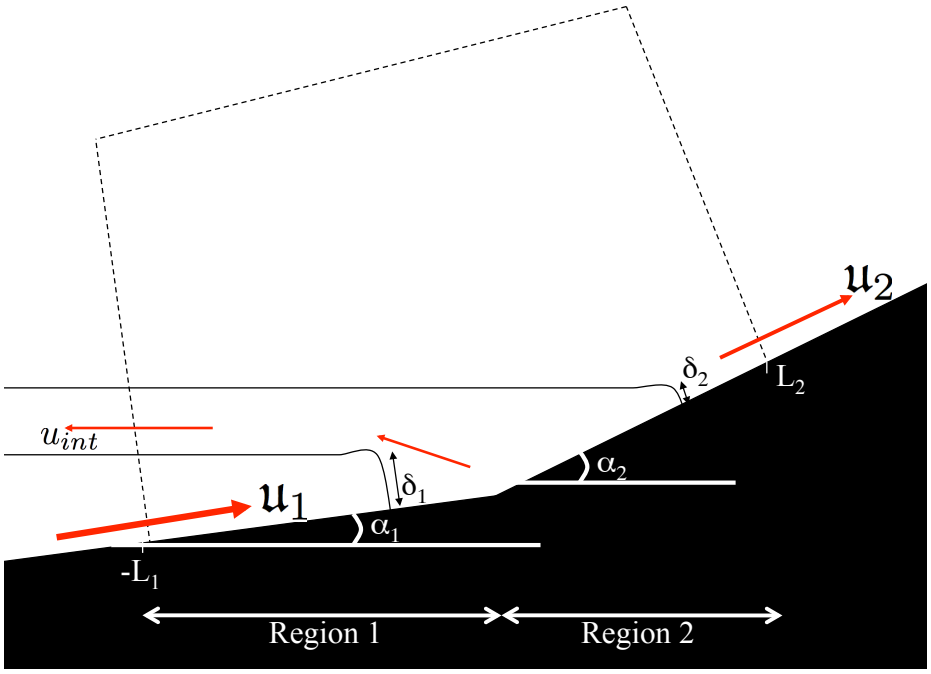

Figure 6: Schematic of dynamics of a diffusion–driven boundary layer over topography with two slopes. In Region 1, the slope has angle α_1, forcing a velocity $\mathfrak{u}_1$. Similarly, in Region 2, the slope has angle α_2, forcing a velocity $\mathfrak{u}_2$. Since the total flux in Region 1 is larger than in Region 2, an intrusion is formed as fluid is forced out of the boundary layer, shown by u_{int}. The dashed line shows a hypothetical box that we can use to make mass, volume, and energy budgets.

boundary layers. The mass flux in a constant slope boundary layer is:

$$M = \int_0^\infty \rho \mathfrak{u} \, \mathrm{d}\eta \tag{25}$$

Assuming a constant stratification, N, and using the density field given in equation (11), and velocity field given in equation (9), this gives a mass flux:

$$M = \rho_0 Q \left(1 - \frac{5}{4} \frac{N^2}{g\gamma} \cos\alpha - \frac{N^2}{g} \xi \sin\alpha \right) \tag{26}$$

Let's consider a mass budget for an imaginary box containing the break in the slope. The box is bounded by the bottom boundary, slope–normal lines at $-L_1$ and L_2, and a horizontal line far enough away from the boundary to be unaffected by boundary layer processes. A box of this type is shown in Figure 6. The total mass balance is now given by:

$$M_1 + M_2 + M_T + M_{int} = 0 \tag{27}$$

M_1 and M_2 are the advective fluxes in the boundary layer on the left and right edges of the box from the bottom boundary layers in Regions 1 and 2. M_T is the diffusive flux across the upper boundary and M_{int} is mass flux in the intrusion. We know what the first three terms are:

$$\begin{aligned}
M_1 &= \rho_0 Q_1 \left(1 - \frac{5}{4} \frac{N^2}{g\gamma_1} \cos\alpha_1 + \frac{N^2}{g} L_1 \sin\alpha_1 \right) \\
M_2 &= -\rho_0 Q_2 \left(1 - \frac{5}{4} \frac{N^2}{g\gamma_2} \cos\alpha_2 - \frac{N^2}{g} L_2 \sin\alpha_2 \right) \\
M_T &= -\kappa \frac{\partial \rho}{\partial z} (L_1 + L_2) \; = \; \rho_0 \frac{N^2 \kappa}{g} (L_1 + L_2)
\end{aligned}$$

The mass flux in the intrusion can be inferred as the residual of the above three mass fluxes:

$$M_{int} = \rho_0 Q_2 \left(1 - \frac{5}{4} \frac{N^2}{g\gamma_2} \cos\alpha_2 \right) - \rho_0 Q_1 \left(1 - \frac{5}{4} \frac{N^2}{g\gamma_1} \cos\alpha_1 \right) \tag{28}$$

Note that M_{int} is independent of the size of the box, given by L_1 and L_2.

The mass that is diffused through the top of the box is balanced by the stratification dependence of the boundary layer fluxes. The mass flux can be nondimensionalized as $M/\rho_0\kappa$, leaving $N^2/g\gamma$ as the only other nondimensional parameter in the budget.

It is also possible to predict the average density of the fluid in the intrusion, ρ_{int}. It is given by:

$$\rho_{int} = \frac{M_{int}}{Q_{int}} = -\frac{M_1 + M_2 + M_T}{Q_1 + Q_2} = \rho_0 \left(1 - \frac{5}{4}\frac{N^2}{g} \underbrace{\frac{Q_1\delta_1 \cos\alpha_1 + Q_2\delta_2 \cos\alpha_2}{Q_1 + Q_2}} \right) \tag{29}$$

Without loss of generality, we choose ρ_0 to be the bottom density at the location of the change in slope. We can see immediately that $\rho_{int} < \rho_0$, because the term indicated with an underbrace is always greater than zero if $\alpha_1 < \alpha_2$. We can similarly bound ρ_{int} as always greater than the density at the top of the boundary layer, where the top is taken to be $\eta\gamma = \pi$, the zero–crossing of the along–slope velocity. The density at the top of the boundary layer is $\rho_0(1 - \frac{N^2\pi\delta}{g\cos\alpha})$, and if one compares this to the size of ρ_{int} given in equation (29), one finds after some rearranging that:

$$Q_1 \left(\frac{\pi\delta}{\cos\alpha} - \frac{5}{4}\delta_1 \cos\alpha_1 \right) > Q_2 \left(\frac{\pi\delta}{\cos\alpha} - \frac{5}{4}\delta_2 \cos\alpha_2 \right) \tag{30}$$

Because the term in the parentheses is always positive, this inequality is always true for $\alpha_1 < \alpha_2$, and ρ_{int} is bound by the densities spanned by the thickness of the boundary layer.

Now that we have developed some expectations about the behavior of the bottom boundary layers in this geometry, we can test them numerically, as described in the next section.

4 Numerical Experiments

To test the ideas proposed in the previous section, we performed a series of numerical experiments using the Regional Ocean Modeling System (ROMS), developed by Shchepetkin and McWilliams (Shchepetkin and McWilliams,

2005). ROMS is a fully non–linear hydrostatic primitive equation model. It has a free surface, and so calculates the barotropic and baroclinic modes separately. ROMS uses topography–following coordinates, also known as σ–coordinates. It was primarily for this reason that ROMS was selected, as σ–coordinates can represent smooth, instead of step–like, topography and so more effectively represent bottom boundary layers. Additionally, ROMS is designed for realistic ocean modeling, so it will be easier to move to more oceanographically relevant configuratons as the research progresses. This includes the capability to run eddy–resolving models.

The numerical experiments presented here use a topography similar to that shown in Figure 6, consisting of two constant slope sections with slopes α_1 and α_2 with a smooth variation between them. In total, there were 60–100 vertical levels, depending on the slope angle and overall water depth in each model run. The vertical resolution increased monotonically as one approached the bottom boundary, with vertical grid spacing varying from about 0.5 m at the bottom to about 15 m at the top. For comparison, the boundary layer scale height δ ranged from 6–40 m. We found that the free surface had a substantial effect even when the water depth was $10 \times \delta$, so all the computations took $35 \times \delta$ as their minimum depth.

Mixing in the model was represented as an explicitly specified eddy diffusivity κ and eddy viscosity ν. The eddy Prandtl number $\mathscr{P}_r = \frac{\nu}{\kappa}$ was assumed to be one. Using eddy mixing coefficients in this simple–minded way is physically problematic because it presupposes a source of energy to stir up turbulent eddies. It is also concerning because, as mentioned in Section 2, the eddy mixing coefficients in the ocean decline as one moves away from the boundary, and this is expected to have an effect on boundary layer dynamics. In spite of these concerns, however, using eddy mixing coefficients based on κ_{canyon} provides a good starting point—numerically straight–forward and physically and observationally plausible. Unfortunately, ROMS does not permit the user to precisely impose a no–slip bottom boundary condition, so the no–slip boundary condition was approximated using a strongly enhanced linear bottom drag. The results were insensitive to the specific value of the coefficient of drag. No surface stress was applied.

The lateral boundaries posed the largest computational problem. To

model a boundary layer with no along–slope variation, we would like to have a domain that is infinitely large in the along–slope direction. However, because the bottom boundary has a slope and there is an overall stratification, it was not possible to use periodic boundary conditions. Ultimately, the lateral boundary conditions that were most successful at reproducing the theoretical solution for a constant slope involved specifying the barotropic momentum at the inflowing boundary and specifying the full, depth–dependent, baroclinic momentum at the outflowing boundary. In order to match the flow to this outgoing boundary condition, a long uninterrupted section of constant slope topography was inserted between the study region and the outflowing boundary. This section was typically 5000 m or longer, 2–10 times the length scale λ for boundary layer development given in equation (13). In an effort to further reduce the effects of the lateral boundaries, the lateral grid spacing was 'telescoped,' increasing exponentially away from the test section. The lateral grid spacing varied from about 65 m to over 900 m.

Radiation conditions were used for the free surface and for the active tracers, namely heat and salt. Though the model included both active tracers, only temperature was used for stratification, and salinity was taken as constant throughout the domain. The stratification was not enforced at either boundary, but rather specified as an initial condition. For the parameter regions explored, the boundary layer was able to reach a steady state before any significant changes had occurred in the stratification. There was no variation in the across–slope direction.

The velocity and density fields produced by the model over a constant slope are shown in Figures 7, 8 and 9. Both the boundary layer velocity and density fields agree with their predicted values to within 2% in the boundary layer. The theory–model mismatch is somewhat larger in the far field, but that is expected because the theory predicts zero anomalies outside the boundary layer. The boundary layer develops over the timescale τ preditcted in equation (12), and maintains a robust steady state.

Once the efficacy of the model was established for a constant slope, a series of fifteen runs were performed in the two–slope configuration, spanning a range of slope angles from $\alpha = 0.001$ to $\alpha = 0.1$. These runs are summarized in the table in Appendix 1. Angles steeper than this range were thought to

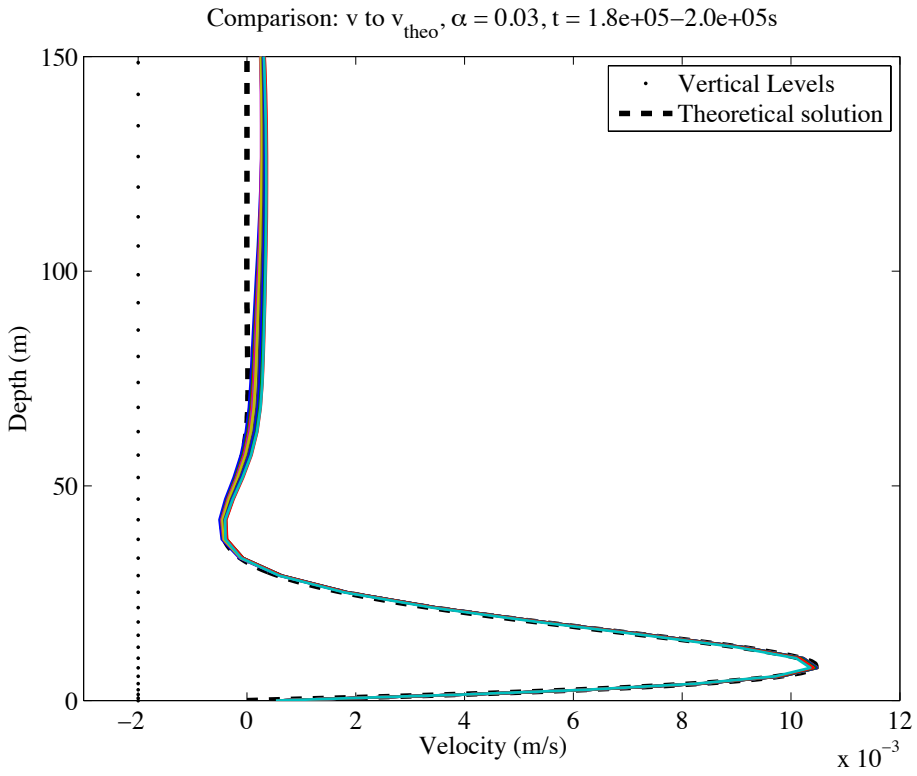

Figure 7: Diffusion Driven Flow over a Constant Slope. The dashed black line indicates the predicted theoretical solution for along–slope velocity, while the colored lines show profiles taken from the numerical solution over the course of several hours. These profiles were taken after more than ten times the adjustment timescale of the boundary layer had elapsed, when the model was at a steady state. The dots on the left side of the plot indicate height of the vertical levels of the grid. The bottom slopes up to the right of the figure.

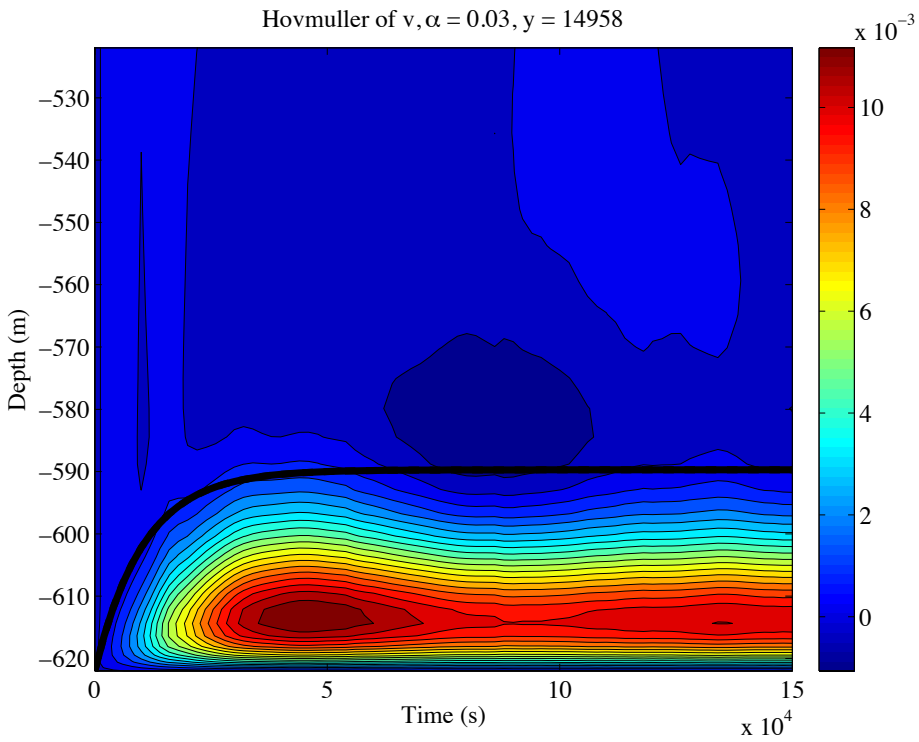

Figure 8: Hovmuller diagram, showing the development of the boundary layer as a function of time. The horizontal axis is time, while the colors show the along–slope velocity. The heavy black line shows the expected growth of the boundary layer thickness, using the time scale derived in equation (12).

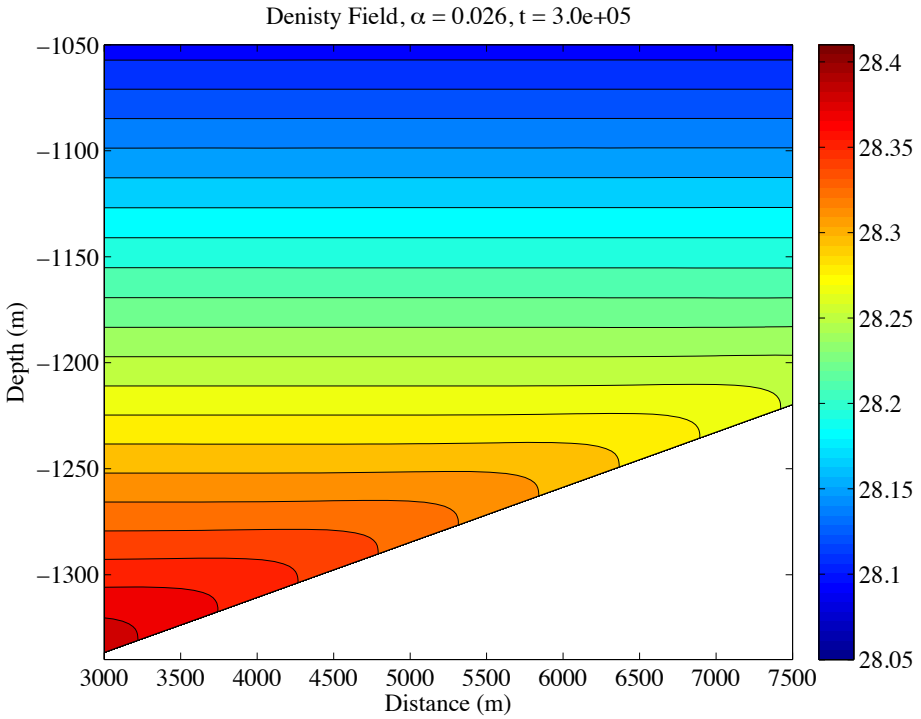

Figure 9: Density field in units of $\sigma = \rho - 1000$ kg m^{-3}. As expected, isopycnals are deflected downward to intersect the slope at a right angle. The density field matches theoretical predictions to within 2%.

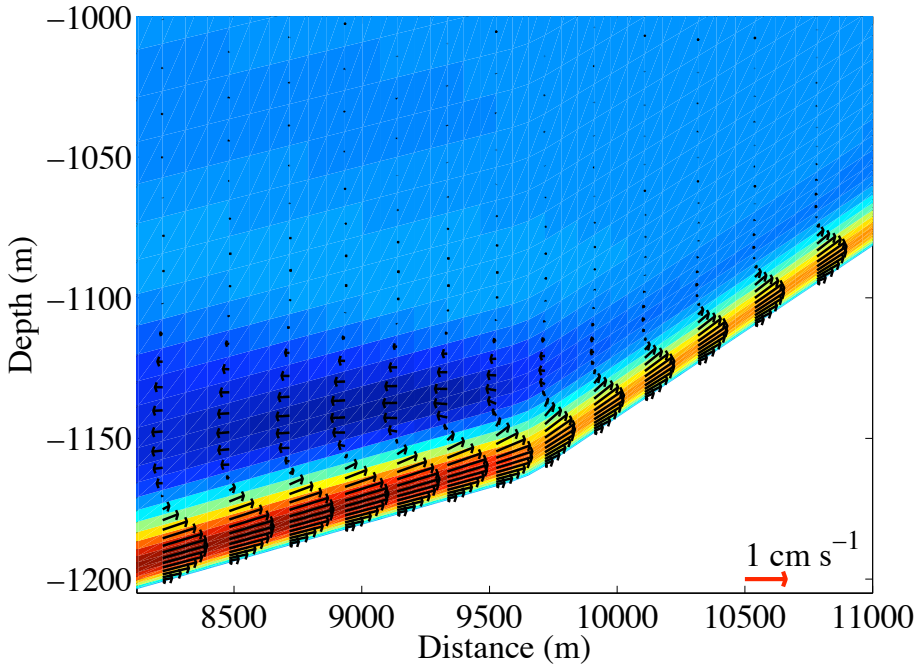

Figure 10: Broken Slope, horizontal velocity section. In addition to the arrows, the background color indicates the horizontal velocity. Note the larger velocities to the left of the change in slope angle, and the counterflowing intrusion flowing left from the change in slope angle.

be not oceanographically relevant. All of the numerical experiments had the basic dynamics described in the previous section, with an inflowing boundary layer of greater mass and volume flux than the outflowing boundary layer, leading to an intrusion of fluid into the far–field. The velocity field of a typical run showing all these features is shown in Figure 10.

The velocity–weighted average densities of the inflowing and outflowing boundary layers are compared to theory in Figure 11. These were calculated by dividing the mass flux by the volume flux in each boundary layer. All the densities are shown relative to ρ_0, which is defined as the bottom density at the change in topographic slope. Again, the agreement is generally satisfactory, though the inflowing boundary layer has a systematically higher density in the numerics than the theory would predict, with a discrepancy of approximately 10^{-2} kg m^{-3}. This may be a result of the low density anomaly from the intrusion that overlies the boundary layer in Region 1, seen in Figure 12. This anomaly reduces the vertical density gradient, so decreases density dif-

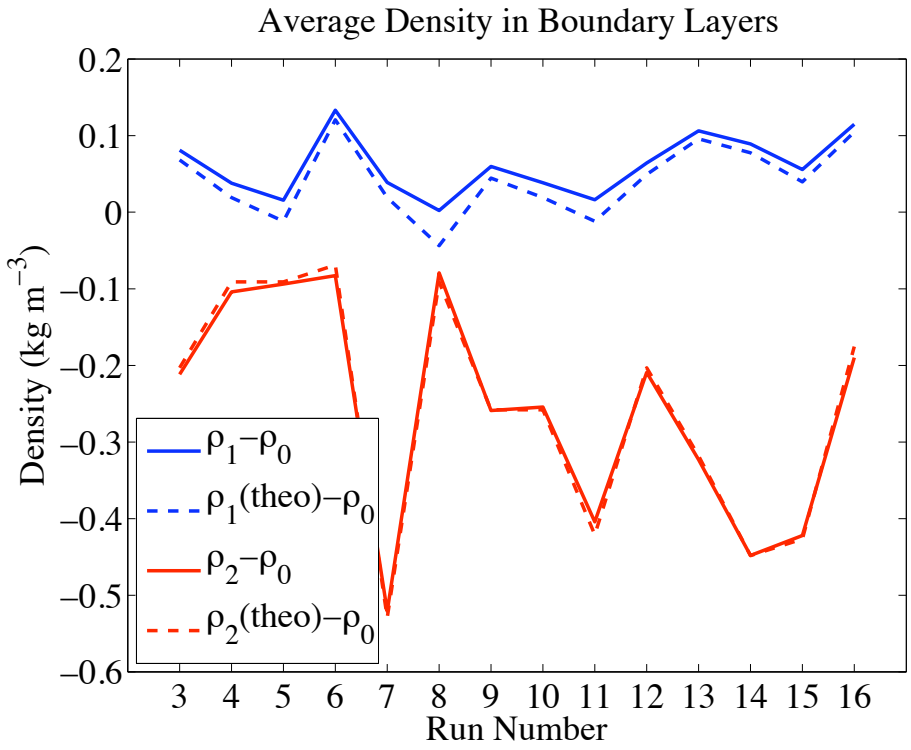

Figure 11: Average density of bottom boundary layers, comparing theory to numerics. The blue lines show the numerics (solid) and theory (dashed) for the average density in the boundary layer in region 1, while the red lines show the same comparison for the boundary layer in region 2. The inflowing (left) boundary layer density is systematically higher than predicted, possibly as a result of the low density anomaly of the fluid intrusion that overlies it.

fusion in the boundary layer, leading to a slightly higher density. However, the diffusive effects of this anomaly should be on the order of 10^{-3} kg m^{-3}, an order of magnitude smaller than the theory–model mismatch that is observed. The low density anomaly over the boundary layer comes from the fluid intrusion forced out of the boundary and into the far field, which can be seen clearly in Figure 12. The intrusion acts to spread the isopycnals, and so will change the interior stratification of a closed basin. It is a mechanism through which boundary mixing can affect the stratification in the far–field.

Quantitative comparisons of the mass budget calculated in the previous section and the numerical results are provided in Figure 13 and Figure 14. The total mass flux in the intrusion calculated numerically agrees with the theoretical prediction to within 5% for all but the smallest slope angles. By normalizing the mass flux it is possible to display this comparison for all numerical experiments on a single figure, Figure 13. In the smallest slope–angle cases, the computational challenges faced in this study were exacerbated. Slower and thicker boundary layers require much larger domains and longer integrations, during which time the stratification erodes. These runs suffer from eroded stratification and much stronger inadvertent boundary impact on the flow from the lateral and surface boundaries. It is worth noting that in all cases, the mass flux out of the boundary layer was of the same order as the total flux in either of the bottom boundary layers. Figure 14 compares ρ_{int} to the prediction and to the range of densities found in the boundary layers, given in equation (29). The numerical mass estimates are frequently lower than the predicted density because the volume flux in the intrusion has been over–estimated. The numerics often feature some small horizontal movement of fluid above the boundary layer and intrusion, up to 20 boundary layer thicknesses δ above the bottom. These are the result of imperfect open lateral boundary conditions. Because the density anomaly ρ' is essentially zero in this area, these horizontal flows carry no net mass flux, but they do carry a little net volume into the control volume. Since there is a small additional Q into the control volume, Q_{int} is a little larger than theory predicts, making the numerical estimate of ρ_{int} lower. Curiously, the numerical experiments showing the best agreement with predictions of he intrusion mass flux M_{int} seem to have the worst agreement with predictions

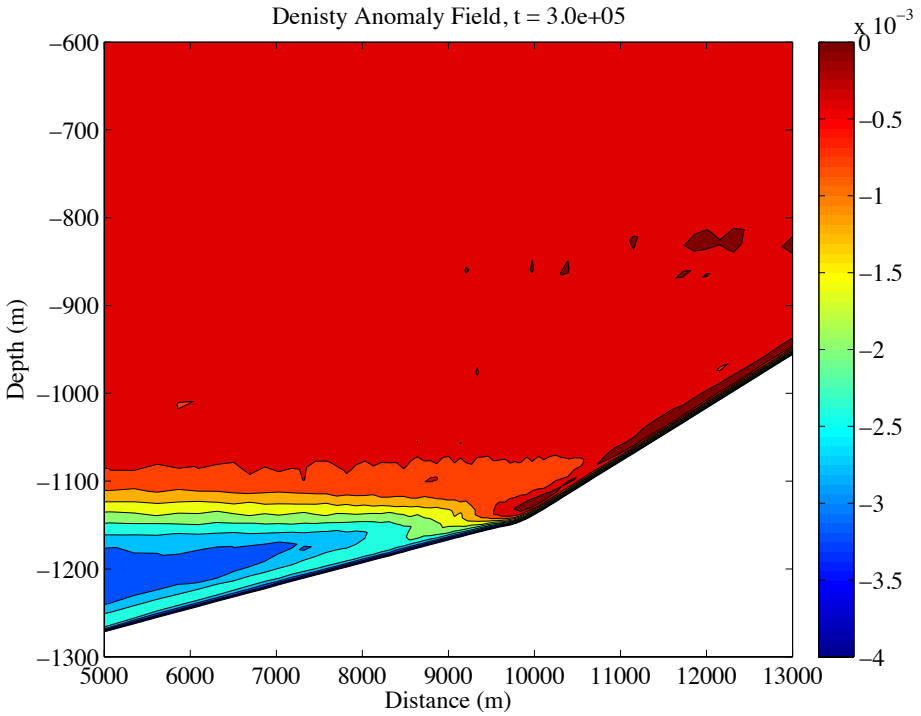

Figure 12: Broken Slope, density anomaly ρ' field. The background stratification has been removed. One can see clearly how the intrusion from the boundary layer has introduced a wedge of heavier fluid (blue in color) into the far field in Region 1, on the left side of the domain. The boundary layer in this simulation is only 20m thick. The contours showing the density anomalies within the boundary layer are tightly clustered near the slope, and difficult to distinguish from one another at this scale. The larger features in this plot are entirely due to the fluid exchange between the boundary layer and the far–field. In the constant slope case, ρ' is zero everywhere outside the boundary layer, so this plot would show no anomaly except inside the boundary layer, the cluster of contours immediately above the bottom.

of the intrusion density.

With the very simple model presented here, we were able to confirm some of our predictions about the behavior of diffusion–driven boundary layers over idealized varying slopes. With the methods established, it will be possible to expand the analysis to more complicated and oceanographically relevant cases.

5 Discussion and Conclusions

The goal of this study was to begin to unpack the physical mechanisms that may underly a fascinating set of observations of deep ocean mixing and flow. The observations of a Mid–Atlantic Ridge flank canyon from the BBTRE centered around both an unexpectedly strong bottom–intensified mean flow and high levels of diapycnal mixing in the canyon. These two features both require a source of energy to drive them, and even the authors who published the data acknowledged that one was unclear. So where did the flow come from, and how does it contribute to the deep ocean mixing budget?

We explored diffusion–driven flow as a possible mechanism to power the along–slope flow on the ocean bottom, using a combination of theory and numerics. This approach is probably most illuminating at either end of the process. By this I mean that it provides a mechanism to drive the along–slope flow with a clearly articulated energy source: potential energy generation through mixing–driven buoyancy flux. This energy source has the potential to break the Chicken–or–Egg cycle of mixing–driven currents coupled to current–driven mixing. At the same time, diffusion–driven flow provides a mechanism for exchange of mixed fluid between the boundary layer and the far–field fluid through the intrusions formed by changes in the slope of the basin bottom. As we showed in our numerical experiments, these intrusions can have as much mass flux as the boundary layer flows themselves. This exchange method is key, as numerous authors have pointed out that boundary mixing can only be a source of buoyancy flux if the boundary layer remains stratified; mixing in an already homogeneous boundary layer will not change its stratification, after all (see, for example, Garrett et al., 1993). So the

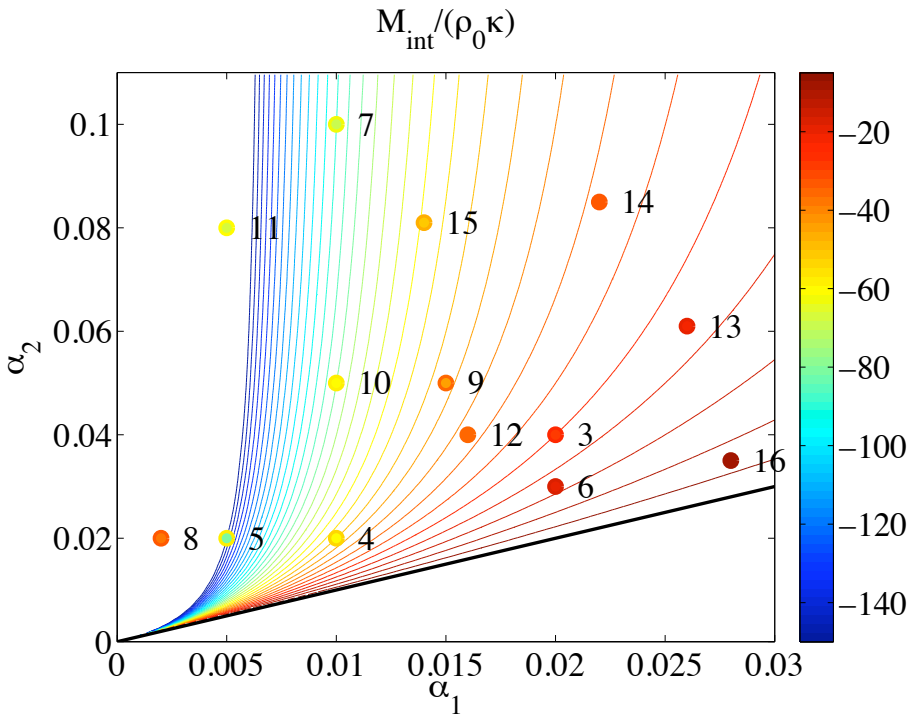

Figure 13: Normalized Mass Fluxes in Intrusions. The contours show the value predicted by the mass budget in equation (28), while the color of the dots show the mass fluxes calculated numerically. The interior of the dot and the rim show two different methods for defining the top and bottom of the intrusion, which yield very similar results. The theory–model mismatch in the smallest slope–angle runs may be a result of computational limitations due to the comparatively long time–scales and large domains needed to reach steady state. Enhanced mixing and vertical shear between the Region 1 boundary layer and the overlying intrusion might further inhibit the full development of the steady–state boundary layer. The remaining nondimensional parameter from equation (28), is $\frac{N^2}{g\gamma} \propto \sqrt{\frac{\kappa}{N}}\frac{N^2}{g} = 2.3 \times 10^{-5}$.

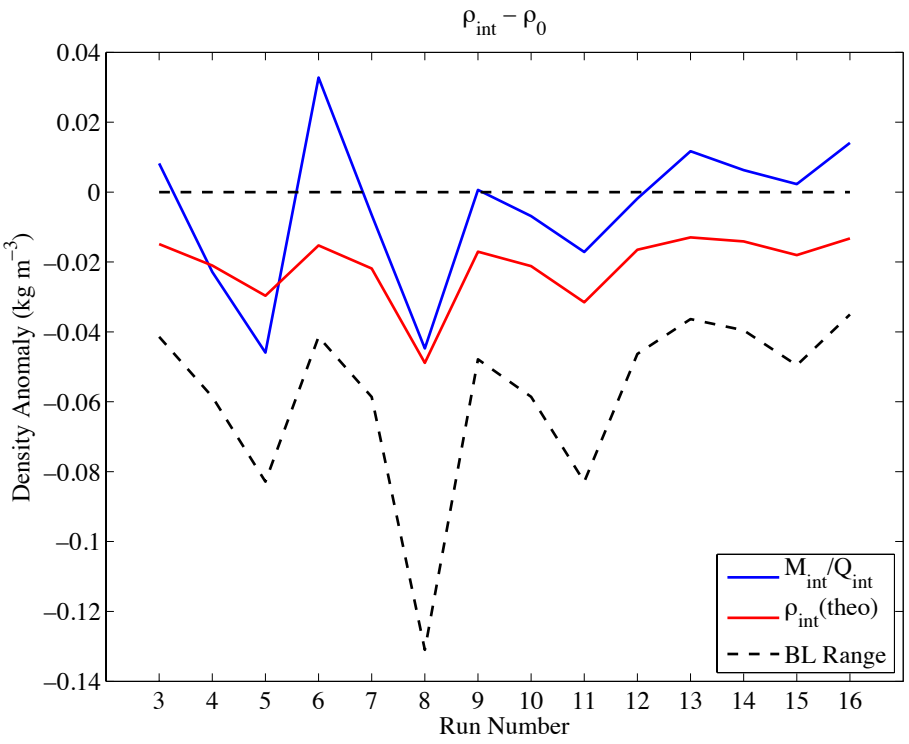

Figure 14: Average density of the fluid in the intrusion, ρ_{int} relative to ρ_0. The blue trace shows the numerical result, the red shows the predicted mass from equation (29) and the dashed lines show the theoretical range of densities spanned by the bottom boundary layer, from $\rho_0(1 - \frac{N^2\pi\delta}{g})$ to ρ_0.

diffusion–driven flow model discussed in this study provides a mechanism for up–slope flow, and for exchange of mixed fluid between the boundary layer and the far field. However, the crucial intermediate processes through which the fluid mixing actually occurs are not detailed, but simply posited by assuming a value of the eddy mixing coefficient, κ_{eddy}. Eddy diffusivities require mechanical stirring, so while we were able to detail the source of energy for the up–slope flow, the energy source for the kinetic energy of stirring remains mysterious. Answering this question is central to understanding if these canyon flows play a dynamically important role in abyssal mixing. As discussed by Wunsch and Ferrari (2004), the deep ocean is a mechanically–driven system, and the most important energy inputs are the stirring of winds and tides. The observations of elevated mixing are impressive, but it is difficult to escape the question of mixing efficiency. The background κ_{eddy} observed in the ocean thermocline is thought to be set by stirring of winds and tides. This input of mechanical energy is converted into available potential energy in the form of the along–canyon slope of isopycnals, creating a pressure gradient. This conversion has some efficiency Γ, which is usually taken to be approximately 0.2 based on laboratory experiments (Turner, 1980; Peltier and Caulfield, 2003). This means that 80% of the kinetic energy is converted to internal heat energy, and 20% to potential energy. In the process described in this study, the available potential energy is then converted back into the kinetic energy of the mean flow, with efficiency $\Gamma \approx 0.5$ in the laminar case from equation (18). Finally, the energy in the mean flow is available to be converted back into potential energy—that is, diapycnal upwelling— through instabilities in the mean flow or topographic interactions. The following table summarizes the energy pathway and the amount of the initial energy input available after each conversion:

KE	$\rightarrow$	PE	$\rightarrow$	KE	$\rightarrow$	PE
Wind/Tides	$\rightarrow$	Isopycnal Slope	$\rightarrow$	Mean Flow	$\rightarrow$	Abyssal Mixing
$\prod \Gamma = 1$	$\rightarrow$	0.2	$\rightarrow$	0.1	$\rightarrow$	0.02

Since every stage in this chain has an efficiency materially less than one, and the total efficiency is the product of the efficiency of each stage, it is difficult to see how the final stage in the chain, when no more than 2% of the energy initially input as winds and tides is still available, could be a sig-

nificant component of the total ocean abyssal energy budget. However, the observational evidence is compelling. In addition to the greatly enhanced mixing observed in the BBTRE, Bryden and Nurser estimate that the 0.1% of the abyssal ocean that is occupied by constrictions and overflows may be sufficient to provide enough mixing to maintain the observed stratification in the ocean because the mixing is so enhanced at these locations (2003). In the history of physical oceanography, most often observations have lead and theory has followed. The phenomenon of greatly enhanced canyon mixing seems sufficiently widespread to merit significant further study.

Looking forward to the future of this work, the first question I would like to answer is whether it is possible for the mechanical energy of stirring to come from the boundary layer flow itself, as Thurnherr's 'mixing–driven' hypothesis might suggest. One simple way to get at this question would be to estimate the potential energy and buoyancy fluxes implied by the hydrographic data collected. As discussed in Section 2, these sources of PE should balance the KE lost to dissipation. If the energy measured in the microstructure dissipation was much larger than the potential energy flux, that would imply that the primary source of mixing in these deep ocean canyons is not driven by the boundary processes discussed in this study. The tracer data from the BBTRE also might provide a better estimate of Q, the volume flux, to compare with the theory.

Another way to approach the question of whether the source of mechanical stirring comes from the canyon flows or is externally imposed is found in additional theoretical work. A stability analysis of the boundary layer flow would show if it were possible for diffusion–driven boundary layers to become unstable and generate turbulence. The Richardson number, $\mathscr{R}_i$ does fall below the instability threshold of $\frac{1}{4}$ in the classical constant–slope solution of Phillips (1970), though this is a necessary and not sufficient condition for instability. The presence of viscosity and a nearby boundary both could act as stabilizing forces. The ROMS simulations performed to date remain stable, however they have Reynolds numbers frequently less than $\mathscr{R}_e \sim 100$ because of the high eddy viscosity. Even if the the boundary layer over a smooth bottom proves to be completely stable, it might be possible for enhanced turbulent diffusivity to be generated by flow over a rough boundary. There

are well–established empirical parametrizations of diffusivity as a function of roughness, for example those of Nikuradse (as reported in Streeter, 1961), that might permit an estimate of the degree of mixing enhancement that the boundary layer current might generate flowing over a rough boundary, as it does in the ocean. If these estimates prove promising, ROMS can be used to perform eddy–resolving numerical experiments on the turbulent boundary layer. Similar work has been done on turbulent Ekman layers (Taylor and Sarkar, 2007), but less attention has been paid to diffusive and sloping boundary layers. All of these are ways to approach the problem of coupling the values of ν and κ to the dynamics of the system instead of imposing them externally, ways of making ν and κ predicted variables instead of constraints.

There is also the larger question of whether roughness parametrizations are the best way to capture the mixing the flow generates. It has been suggested that the primary source of enhanced bottom mixing is due overflows, constrictions, and sills in the canyons. Is there a way to couple the stratified boundary layer model proposed here to hydraulic models of these overflows? If so, that might answer another important question that the BBTRE data suggest, namely what is balancing the along–canyon pressure gradient? One candidate is form drag, which is greatly enhanced around overflows, but not over roughness. One idealized model of hydraulically–controlled overflows is shown in Appendix 2 to this work.

In addition to the question of turbulence generation, there are a number of other interesting way to continue the work begun here so as to better model and understand the dynamics of diffusion–driven flow and how they might play out in the real ocean. First, it would be interesting to deepen the energy budget presented here to include a thermodynamic analysis of the mechanism by which internal energy is converted into kinetic energy by density diffusion. It would also be useful to extend the theory here to account for the effects of rotation. The canyon studied in the BBTRE is narrower than the local Rossby radius of deformation, which is why it seemed sensible to begin with a non–rotating theory. However, it may be relatively straight–forward to include rotation simply by modeling the canyon flow as a channel flow. In that case, it might be possible for the flow to be in geostrophic balance

across the canyon while maintaining the dynamics already described along the canyon, as described for hydraulic channel flows in Pratt and Whitehead (2007). Additionally, it would be interesting to see how boundary layers respond to more complicated topographies than the simple broken slope described here. What happens when you have both positive and negative slope curvature? How does the scale of the curvature affect the exchange flow with the interior? What kind of exchange flow occurs over topography that matches the spectral characteristics of the ocean bottom? Finally, it might be informative to simulate some of the flows discussed here in the laboratory. The generation of a diffusion–driven flow over a non–constant slope would not be difficult, but it does not appear to have been tried yet in the published literature, either in laminar or turbulent boundary layers.

6 Appendix 1: Summary of Numerical Experiments

Run Number	α_1	α_2	Vertical Levels	Depth (m)	Duration (s)
DDF6-02	0.02	0.02	90	1100	2×10^5
DDF6-03	0.02	0.04	90	1100	2×10^5
DDF6-04	0.01	0.02	80	750	2×10^5
DDF6-05	0.005	0.02	80	700	2×10^5
DDF6-06	0.02	0.03	95	950	2×10^5
DDF6-07	0.01	0.1	105	1165	2×10^5
DDF6-08	0.002	0.02	60	670	3×10^6
DDF6-09	0.015	0.05	70	1055	4×10^5
DDF6-10	0.01	0.05	70	1005	4×10^5
DDF6-11	0.005	0.08	70	1452	3×10^5
DDF6-12	0.016	0.04	75	1061	4×10^5
DDF6-13	0.026	0.061	75	1424	3×10^5
DDF6-14	0.022	0.085	75	1685	3×10^5
DDF6-15	0.014	0.081	75	1555	3×10^5
DDF6-16	0.028	0.035	75	1118	3×10^5

7 Appendix 2: Overflow Calculation

This appendix presents an idealized model of mixing by flow over periodic sills. It is included with this Masters thesis as an example of the kind of analysis that might be useful in explaining the sources of mixing observed in abyssal ocean canyons. It is uses the shallow–water equations to describe an unstratified, inviscid flow. Unfortunately, it may not be possible to directly integrate this model of mixing and energy dissipation with the diffusion–driven flow model discussed in this work, which is dominated by stratification and diffusion effects. However, it points to a need for further work on the actual mechanisms of mixing in submarine canyons. It is also noteworthy for being a periodic inviscid flow, whose only drag comes from form drag.

Begin by considering a two–dimensional topography, periodic in an along–stream coordinate y, with spatial wavelength λ. This topography is overlaid onto a constant inclination angle α, as shown in Figure 15. Can we have a strictly periodic inviscid flow descending over this topography? Assume it is hydraulically controlled at each sill. Over each period, the gravitational potential energy associated with descending a height $\alpha\lambda$ is converted to kinetic energy of the flow, which is dissipated at the hydraulic jump.

We can calculate the energy dissipation at the jump using conservation rules (Pratt and Whitehead, 2007), begining with the conservation of flux:

$$Q = v_a d_a = v_b d_b \tag{31}$$

This is true for any locations y_a and y_b, but we'll be most interested in the dynamics between immediately above and immediately below the jump, as labeled in Figure 15. We assume that the volume flux Q is known. The next conservation relationship comes from momentum. Integrate pressure over the flow cross–section to find:

$$v_a^2 d_a + \frac{1}{2} g d_a^2 = v_b^2 d_b + \frac{1}{2} g d_b^2 \tag{32}$$

Finally, the Bernoulli function B is the total amount of energy in the flow at a given location. It is the conserved quantity in the shallow water equation, here shown with a known imposed surface pressure, p_0, varying in

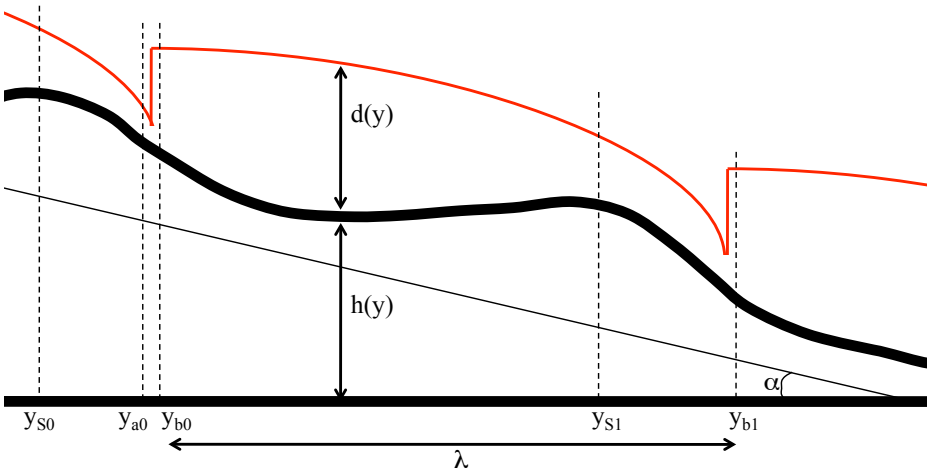

Figure 15: Definition of variables. The thick black line shows the topography, given by the function $h(y)$. It has overall slope α and spatial period λ. The water depth is given by the red line, showing an hydraulic jump after each local topographic maximum.

the along–stream y direction:

$$\underbrace{v\frac{\partial v}{\partial y}}_{0} + \underbrace{g\frac{\partial h}{\partial y}}_{+} + \underbrace{g\frac{\partial d}{\partial y}}_{0} + \underbrace{\frac{1}{\rho}\frac{\partial p_0}{\partial y}}_{-} = 0 \tag{33}$$

The underbraces indicate the sign we expect each term to take over one wavelength of the periodic topography if the flow is uphill. Since the solution is periodic, v and d should not change over one wavelength, giving not net change and zero derivative. The shallow water equation (33) gives a conserved quantity:

$$B = \frac{1}{2}v^2 + gd + gh + \frac{1}{\rho}p_0 \tag{34}$$

B must be conserved everywhere that equation (33) is true. In our case, that means that it is conserved everywhere except right at the hydraulic jump. Since energy must be conserved overall, the amount of energy dissipated at the hydraulic jump must be equal to the change in the Bernoulli function over one wavelength. That is:

$$B(y_{a0}) - B(y_{b0}) = B(y_{b0}) - B(y_{b1}) \tag{35}$$

Since the flow profile (v, d) is identical for all y_b, this implies:

$$\begin{aligned} B(y_{a0}) - B(y_{b0}) &= g\big(h(y_{b0}) - h(y_{b1})\big) + \frac{1}{\rho}\big(p_0(y_{b0}) - p_0(y_{b1})\big) \\ &= g\Delta h + \frac{1}{\rho}\Delta p_0 \end{aligned} \tag{36}$$

Δh and Δp_0 are the change in pressure and topographic height over one spatial wavelength λ, and are both known quantities. Similarly, we can expand the LHS of the above equation:

$$\frac{1}{2}v_a^2 + gd_a + \cancel{gh(y_{a0})} + \cancel{\frac{1}{\rho}p_0(y_{a0})} - \Big(\frac{1}{2}v_b^2 + gd_b + \cancel{gh(y_{b0})} + \cancel{\frac{1}{\rho}p_0(y_{b0})}\Big) = g\Delta h + \frac{1}{\rho}\Delta p_0$$

$$\frac{1}{2}\Big(v_a^2 - v_b^2\Big) + g\Big(d_a - d_b\Big) = g\Delta h + \frac{1}{\rho}\Delta p_0 \tag{37}$$

The pressure and topographic terms cancel because the hydraulic jump is so sharp that $y_{a0} \approx y_{b0}$, and the topography and pressure varies on scales much longer than the width of the jump. We can combine equation (37) with our conservation of flux and momentum equations (31) and (32) to directly relate the water depth immediately before and after the hydraulic jump, d_a and d_b:

$$\frac{(d_b - d_a)^3}{4d_a d_b} = \Delta h + \frac{1}{g\rho}\Delta p_0 \tag{38}$$

We need one further constraint to determine the depth of the fluid everywhere in terms of known quantities. We know that the flow is hydraulically controlled, and as long as there is no bottom friction and p_0 is monotonic, the control section must be at the local maximum topographic height. That is the Froude number is one at y_s:

$$F_r = \frac{v_s^2}{gd_s} = 1 \tag{39}$$

We can therefore express both v_s and d_s in terms of the known flux $Q = vd$:

$$v_s = (gQ)^{1/3} \qquad ; \qquad d_s = \left(\frac{Q^2}{g}\right)^{1/3} \tag{40}$$

This gives us the Bernoulli function at the sill purely in terms of known quantities:

$$B_s = \frac{3}{2} g^{2/3} Q^{2/3} + gh(y_s) + \frac{1}{\rho} p_0(y_s) \tag{41}$$

Since the Bernoulli function is conserved everywhere except at the hydraulic jump, if we know $B(y_{s1})$, we know B everywhere from y_{b0} to y_{a1}. By equation (34), we know the fluid depth and velocity in that range. Taking the calculated depth at y_{a1} and plugging it into equation (37), we get $d(y_{b1})$. At every point, we can get v from d using the conservation of flux Q. Since the solution is periodic, we now know everything about this flow. Unfortunately, since equation (37) is a non–linear third order polynomial, it's not very easy to express the depth or velocity in closed form. However, it is easy to plot it. Following are some figures showing a pressure–driven flow up a slope with sinusoidal sills (Figure 16) and gravity–driven flow down a slope with sawtooth sills (Figure 17).

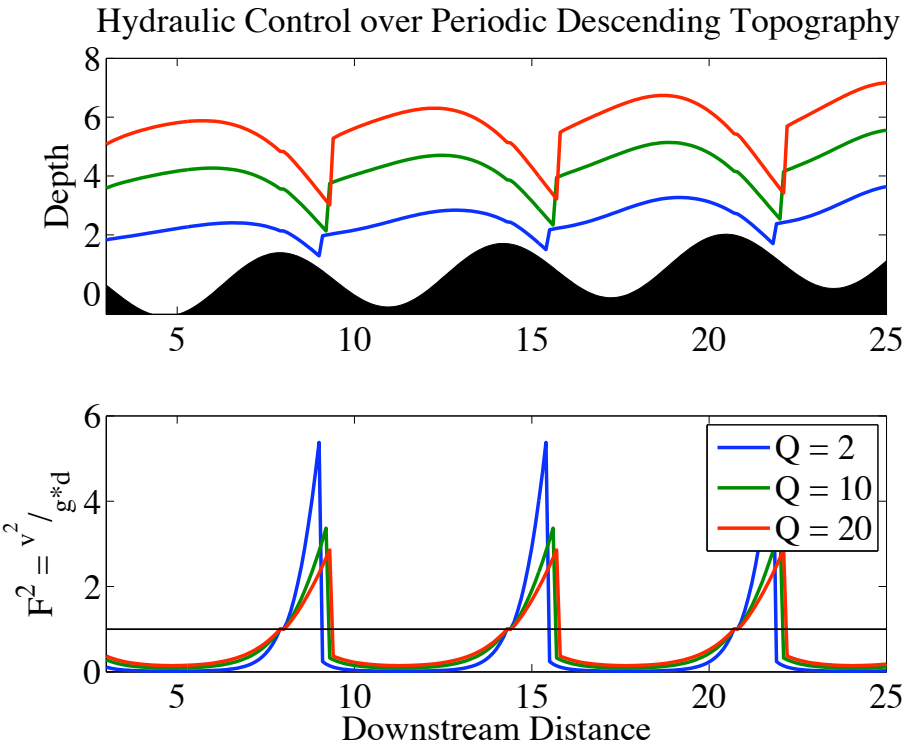

Figure 16: Depth and Froude number for three mass fluxes over sinusoidal topography. Note the weak dependence of the jump location on the flux; this makes calculating the form drag difficult. In this example there is an imposed surface pressure with a linear gradient driving the flow up the hill, from left to right.

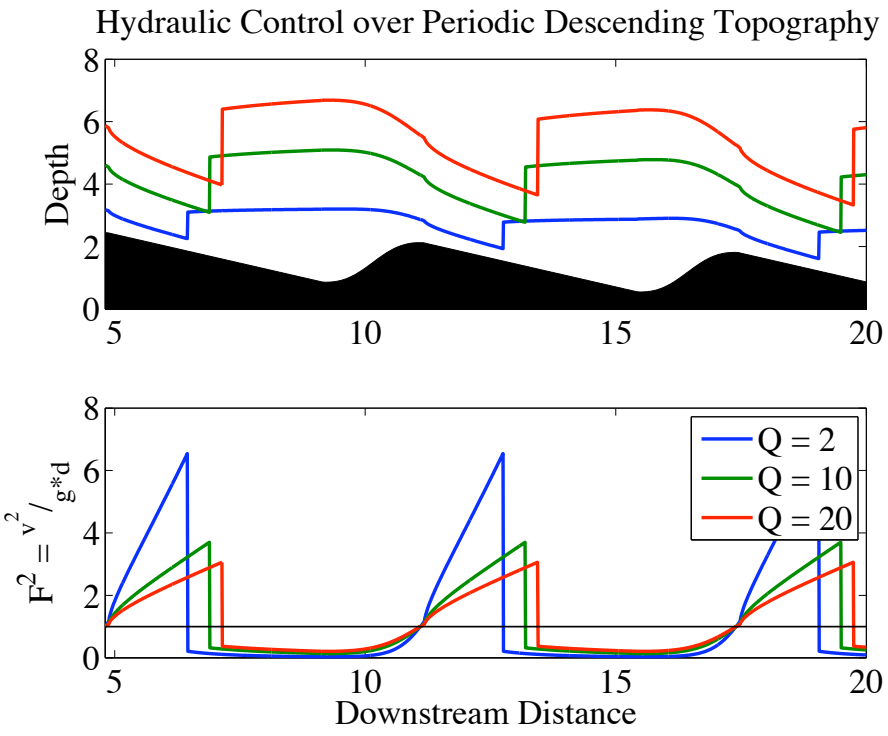

Figure 17: Depth and Froude number for three mass fluxes over sawtooth topography. In this example there is no imposed surface pressure; all the energy dissipated in the jumps comes from loss of gravitational potential energy, as the fluid flows from left to right.

References

H. L. Bryden and A. J. G. Nurser. Effects of strait mixing on ocean stratification. *Journal of Physical Oceanography*, 33:1870–1872, 2003.

C. Garrett, P. MacCready, and P. B. Rhines. Arrested Ekman layers: Rotating stratified flow near a sloping boundary. *Annual Reviews of Fluid Mechanics*, 25:291–323, 1993.

N. G. Hogg, P. Biscaye, W. Gardner, and W. J. Schmitz, Jr. On the transport and modification of Antarctic Bottom Water in the Vema Channel. *Journal of Marine Research*, 40:231–263 (suppl.), 1982.

J. R. Ledwell, E. T. Montgomery, K. L. Polzin, L. C. St. Laurent, R. W. Schmitt, and J. M. Toole. Evidence for enhanced mixing over rough topography in the abyssal ocean. *Nature*, 403:179 – 182, January 2000.

M. Y. Morris, M. M. Hall, L. C. St. Laurent, and N. G. Hogg. Abyssal mixing in the Brazil Basin. *Journal of Physical Oceanography*, 31:3331–33348, 2001.

W. H. Munk. Abyssal recipes. *Deep-Sea Research*, 13:707–730, 1966.

T. Peacock, R. Stocker, and J. M. Aristoff. An experimental investigation of the angular dependence of diffusion-driven flow. *Physics of Fluids*, 16(9): 3503–3505, 2004.

W. R. Peltier and C. P. Caulfield. Mixing efficiency in stratified shear flows. *Annual Review of Fluid Mechanics*, 35:135–167, 2003.

O. M. Phillips. On flows induced by diffusion in a stably stratified fluid. *Deep-Sea Research*, 17:435–443, 1970.

O. M. Phillips, J.-H. Shyu, and H. Salmun. An experiment on boundary mixing: Mean circulation and transport rates. *Journal of Fluid Mechanics*, 173(473-499), 1986.

K. L. Polzin, K. G. Speer, J. M. Toole, and R. W. Schmitt. Intense mixing of Antarctic bottom water in the equatorial Atlantic ocean. *Nature*, 380: 54–57, March 1996.

K. L. Polzin, J. M. Toole, J. R. Ledwell, and R. W. Schmitt. Spatial variability of turbulent mixing in the abyssal ocean. *Science*, 276:93–96, April 1997.

L. J. Pratt and J. A. Whitehead. *Rotating Hydraulics*. Springer Verlag, 2007.

A. F. Shchepetkin and J. C. McWilliams. The Regional Ocean Modeling System (ROMS): a split-explicit, free-surface, topography-following-coordinate oceanic model. *Ocean Modelling*, 9:347–404, 2005.

L. C. St. Laurent and A. M. Thurnherr. Intense mixing of lower thermocline water on the crest of the Mid-Atlantic Ridge. *Nature*, 448:680–683, August 2007.

L. C. St. Laurent, J. M. Toole, and R. W. Schmitt. Buoyancy forcing by turbulence above rough topography in the abyssal Brazil Basin. *Journal of Physical Oceanography*, 31:3476–3495, December 2001.

V. L. Streeter, editor. *Handbook of Fluid Dynamics*. McGraw-Hill, 1961.

J. R. Taylor and S. Sarkar. Internal gravity waves generated by a turbulent bottom Ekman layer. *Journal of Fluid Mechanics*, 590:331–354, 2007.

S. A. Thorpe. Current and temperature variability on the continental slope. *Philosophical Transactions of the Royal Society London Series A*, 323:471–517, 1987.

A. M. Thurnherr and K. G. Speer. Boundary mixing and topographic blocking on the Mid-Atlantic Ridge in the South Atlantic. *Journal of Physical Oceanography*, 33:848–862, April 2003.

A. M. Thurnherr, L. C. St. Laurent, K. G. Speer, J. M. Toole, and J. R. Ledwell. Mixing associated with sills in a canyon on the midocean ridge flank. *Journal of Physical Oceanography*, 35:1370–1381, August 2005.

A. M. Thurnherr, G. Reverdin, P. Bouruet-Aubertot, L. C. St. Laurent, A. Vangriesheim, and V. Ballu. Hydrography and flow in the Lucky Strike segment of the Mid-Atlantic Ridge. *Journal of Marine Research*, 66(3): 347–372, 2008.

J. M. Toole. Temporal characteristics of abyssal finescale motions above rough bathymetry. *Journal of Physical Oceanography*, 37:409–427, March 2007.

J. S. Turner. *Buoyancy Effects in Fluids*. Cambridge University Press, 1980.

G. K. Vallis. *Atmospheric and Oceanic Fluid Dynamics*. Cambridge University Press, 2006.

A. W. Woods. Boundary-driven mixing. *Journal of Fluid Mechanics*, 226: 625–654, 1991.

C. Wunsch. On oceanic boundary mixing. *Deep-Sea Research*, 17:293–301, 1970.

C. Wunsch and R. Ferrari. Vertical mixing, energy, and the general circulation of the oceans. *Annual Reviews of Fluid Mechanics*, 36:281–314, 2004.